Analysis and algorithms for a regularized cauchy problem arising from a non-linear elliptic PDE for seismic velocity estimation

M.K. Cameron [a,*], S.B. Fomel [b], J.A. Sethian [c]

[a] Courant Institute of Mathematical Science, Department of Mathematics, New York University, 251 Mercer Street, New York, NY 10012, United States
[b] Bureau of Economic Geology, The University of Texas at Austin, University Station, Box X, Austin, TX 78713-8924, United States
[c] Department of Mathematics, University of California, Berkeley, 970 Evans Hall, Berkeley, CA 94720, United States

ABSTRACT

In the present work we derive and study a non-linear elliptic PDE coming from the problem of estimation of sound speed inside the Earth. The physical setting of the PDE allows us to pose only a Cauchy problem, and hence is ill-posed. However, we are still able to solve it numerically on a long enough time interval to be of practical use. We used two approaches. The first approach is a finite difference time-marching numerical scheme inspired by the Lax–Friedrichs method. The key features of this scheme is the Lax–Friedrichs averaging and the wide stencil in space. The second approach is a spectral Chebyshev method with truncated series. We show that our schemes work because of (i) the special input corresponding to a positive finite seismic velocity, (ii) special initial conditions corresponding to the image rays, (iii) the fact that our finite-difference scheme contains small error terms which damp the high harmonics; truncation of the Chebyshev series, and (iv) the need to compute the solution only for a short interval of time. We test our numerical schemes on a collection of analytic examples and demonstrate a dramatic improvement in accuracy in the estimation of the sound speed inside the Earth in comparison with the conventional Dix inversion. Our test on the Marmousi example confirms the effectiveness of the proposed approach.

© 2009 Elsevier Inc. All rights reserved.

1. Introduction

In the present work we derive and study a non-linear elliptic PDE for seismic velocity estimation from time migration. The physical setting allows us to pose only a Cauchy problem and this is ill-posed. Nonetheless, because this PDE provides an inexpensive way to estimate the sound speed inside the Earth, an attempt to provide some sort of solution is worthwhile. We begin with a short overview.

Seismic data are the records of the sound wave amplitudes $P(S, G, t)$ where S is the source position, G is the receiver position, and t is the time. Seismic reflection imaging can be viewed as a procedure of obtaining the amplitude at the subsurface point (x, y, z) from the data points (S, G, t), where $(x, y, z) = R$ is the reflection point of the ray path from the source S to the receiver G (see Fig. 1).

---

* Corresponding author. Tel.: +1 212 998 3148.
  E-mail addresses: cameron@cims.nyu.edu (M.K. Cameron), sergey.fomel@beg.utexas.edu (S.B. Fomel), sethian@math.berkeley.edu (J.A. Sethian).
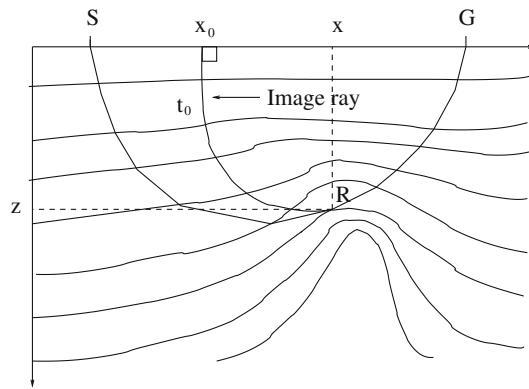
Fig. 1. The raypath between the source *S*, the reflection point *R* and the receiver *G*; the image ray from the reflection point *R* and the time and depth coordinates of the point *R*.

To obtain an accurate image at the reflection point $R = (x, y, z)$, one needs to sum up all of the recorded responses from the point *R* in the data domain with certain weights. Such a weighted summation of the amplitudes in the data domain is the essence of the so-called *Kirchhoff prestack depth migration* [30]. In order to extract the responses from every single reflection point from the set of the recorded data, one needs to know the traveltimes from every source *S* to every reflection point $R = (x, y, z)$ and from every reflection point *R* to every receiver *G*. For computing such traveltimes, one needs to have a *velocity model in depth* $v(x, y, z)$, i.e, the speed of the propagation of the seismic waves inside the earth. We call such a model *seismic velocity*. In the case of an isotropic seismic velocity, one can solve the eikonal equation

$$|\nabla T(x, y, z)|^2 = \frac{1}{v^2(x, y, z)} \tag{1}$$

to find the desired traveltimes.

The major problem of seismic imaging is that such a velocity model is hard to build. A number of powerful automatic velocity estimation methods have been proposed. This includes reflection tomography [29], stereotomography [14], migration velocity analysis [26,27], and differential semblance optimization [25]. However, these methods typically involve considerable computational expense and rely on a good initial approximation. Numerical studies of the well-known Marmousi data [28] demonstrate that, in the absence of a good initial guess, none of the modern approaches are fully reliable. The approach which this paper is concerned with is computationally cheap and requires no initial guess. It can provide an initial guess for the approaches listed above.

In [3] we formulated an inverse problem of finding the seismic velocities from the so-called "Dix velocities", and showed that it is ill-posed in the sense that small perturbations in the Dix velocity may lead to big changes in the seismic velocity. Nevertheless, in that paper we also attempted a regularized reconstruction and developed two numerical approaches to solve the problem. Since the estimated seismic velocity was used in the depth migration, only for the computation of the traveltimes, and was not used for the delineation of the subsurface reflectors, smoothing of the velocity model did not lead to significant errors.

The key problem in these approaches hinged on the estimation of the second derivatives of the unknown velocity. We used a least squares polynomial approximation to regularize the solution. However, choosing the degree of the least squares polynomials was sensitive. If the degree was too high, oscillations developed; if it was too low, the solution was inexact.

In this work, we develop novel inversion methods which involve neither the least squares polynomial approximation nor ray tracing. Our results include the following:

- In the theoretical part, we derive a partial differential equation for *Q* which is the geometrical spreading of image rays [11], and involves only the Dix velocity and its derivatives with respect to the starting surface points and time. This reformulated PDE reveals the nature of the instabilities in the problem in hand. The PDE is elliptic, and the physical setting allows us to pose only a Cauchy problem, which is known to be ill-posed. Furthermore, the fact that the PDE involves not only the Dix velocity itself but also its first and second derivatives leads to high sensitivity to the input data. This makes the ill-posedness analysis given in [3] unsurprising: a small perturbation of the Dix velocity can produce a significant corresponding change in its second derivative, and can lead to a considerable change in the seismic velocity.
- Despite the fact that problem is ill-posed, we show that we are still able to find a way to compute the solution:
  - First, we develop a finite difference time-marching numerical scheme and compute a solution on the required interval of time. Our numerical scheme is motivated by the Lax–Friedrichs [15] method for hyperbolic conservation laws as a building block.
  - Second, we adjust a spectral Chebyshev method for the problem in-hand. We truncate the Chebyshev series to cut off the growing high harmonics in this case.

• We generalize the PDE and our finite difference numerical scheme for the 3D, and test our numerical techniques on a collection of synthetic examples, demonstrating that we are able to restore the seismic velocity quite accurately. Results are compared with the standard Dix estimate, and demonstrate that the Dix estimate might differ qualitatively from the original velocity while our correction gives a significant and qualitative improvement to the Dix estimate.

The organization of this paper is as follows: in Section 2, we provide background equations and setting. In Section 3, we derive our main equation for the time evolution of the geometrical spreading of the image rays. In Section 4, we demonstrate that we are able to solve the resulting equation with good accuracy despite being a Cauchy problem for an elliptic equation. In Section 5, we provide an explanation why we are able to do so. In Section 6, we test our approach on the Marmousi example. In Section 7, we derive a similar equation for the 3D. In Section 8, we describe a 3D numerical scheme and provide synthetic examples.

2. Background

While depth-domain seismic imaging (a.k.a. depth migration) became practical due to powerful computing resources, time-domain seismic imaging (a.k.a. time migration) [30] has been a mainstay for decades starting even in the "precomputer era". Nowadays time migration is still the main tool in many regions of the world and often the first step in the workflow leading to depth imaging. Time migration avoids the need for velocity model by making an approximation. One common approximation used in the prestack time migration is the following [30]. The traveltime $T(S, R) + T(R, G)$ from the source S to the reflection point R and then to the receiver R is given by

$$T(S, R) + T(R, G) \approx T(S, G, \mathbf{x}_0, t_0) = \sqrt{\frac{t_0^2}{4} + \frac{|\mathbf{x}_0 - S|^2}{v_m^2(\mathbf{x}_0, t_0)}} + \sqrt{\frac{t_0^2}{4} + \frac{|\mathbf{x}_0 - G|^2}{v_m^2(\mathbf{x}_0, t_0)}}. \tag{2}$$

Here, $\mathbf{x}_0$ and t_0 are effective parameters of the subsurface point R, t_0 is the shortest traveltime from the point R to the Earth surface, $\mathbf{x}_0$ is the escape location of the fastest ray, and $(\mathbf{x}_0, t_0)$ are the so-called *time coordinates* of the subsurface point R, while (x, y, z) are its *depth coordinates*. The fastest ray, which arrives normal to the surface, was named the *image ray* by Hubral [10], as its escape location is the image of the subsurface point R on the surface. Fig. 1 provides an illustration for the connection between the image ray and the time and depth coordinates.

The parameters $v_m(\mathbf{x}_0, t_0)$ in Eq. (2) are chosen in the process of time migration by an optimal (e.g. least squares) fit. They have the physical dimension of the velocity: due to this fact, they are often called the *migration velocities*.

If the seismic velocity v is constant, the raypaths from the source S to the reflection point R and from R to the receiver G are straight and the image ray from R is vertical (Fig. 1). Then Eq. (2) follows from the Pythagorean theorem and provides the exact expression for the traveltime. In this case, the migration velocity v_m equals the constant seismic velocity v.

The connection between the migration velocity and the seismic velocity in the case of the laterally homogeneous seismic velocity, i.e. $v(x, y, z) \equiv v(z)$, was developed by Dix [8]. He proved that if the *offsets* (the distances between the source and the receiver) are small, the migration velocity $v_m(\mathbf{x}_0, t_0)$ is the root-mean-square (RMS) velocity [8], given by

$$v_m(t_0) = \sqrt{\frac{1}{t_0} \int_0^{t_0} v^2(z(\tau)) d\tau}. \tag{3}$$

Therefore, the seismic velocity in the time coordinates is given by

$$v(\mathbf{x}_0, t_0) = \sqrt{\frac{\partial}{\partial t_0} \left(t_0 v_m^2(\mathbf{x}_0, t_0) \right)}. \tag{4}$$

Since the image rays are vertical in this case, the conversion from the time coordinates $(\mathbf{x}_0, t_0)$ can be accomplished by the vertical stretch

$$z(\mathbf{x}_0, t_0) = \int_0^{t_0} v(\mathbf{x}_0, \tau) d\tau, \tag{5}$$

and hence $v(x, y, z) = v(\mathbf{x}_0, z(\mathbf{x}_0, t_0))$ where $(x, y) = \mathbf{x}_0$.

The Dix formulae (4) and (5) are still in common practice even if the offsets are not small and the seismic velocity changes laterally. The violation of the assumption of the small offsets does not lead to a significant error [30]. However, the violation of the lateral homogeneity assumption leads to significant errors, both in the positioning in depth [10] and in the seismic velocity itself [3].

2.1. Seismic and time migration velocities

In a series of papers [2–5], we derived the theoretical relationships between the Dix velocities and the seismic velocities: in 2D [2] and 3D [3–5]. These results were reconfirmed in [12]. The seismic velocities and the Dix velocities are connected

through the quantity **Q**, which represents the geometrical spreading of image rays. **Q** is a scalar in 2D and a 2×2 matrix in 3D. The simplest way to introduce **Q** is the following. Trace an image ray $\mathbf{x}(\mathbf{x}_0, t)$, where $\mathbf{x}_0$ is the starting surface point and t is the traveltime. Call this ray *central*. Consider a small tube of rays around it. All these rays start from a small neighborhood $d\mathbf{x}_0$ of the point $\mathbf{x}_0$ perpendicular to the earth surface. Thus, they represent a fragment of a plane wave propagating downward. Consider the fragment of the wave front defined by this ray tube at time t_0. Let $d\mathbf{q}$ be the fragment of the tangent to the front at the point $\mathbf{x}(\mathbf{x}_0, t_0)$ reached by the central ray at time t_0, bounded by the ray tube (Fig. 2). Then, in 2D, Q is the derivative $Q(x_0, t_0) = \frac{dq}{dx_0}$. In 3D, **Q** is the matrix of the derivatives $\mathbf{Q}_{ij}(\mathbf{x}_0, t_0) = \frac{d\mathbf{q}_i}{d\mathbf{x}_{0j}}, i, j = 1, 2$, where derivatives are taken along certain mutually orthogonal directions $\mathbf{e}_1, \mathbf{e}_2$ [19,7,18].

In [3], we prove that

$$v_{Dix}(x_0, t_0) \equiv \sqrt{\frac{\partial}{\partial t_0}(t_0 v_m^2(x_0, t_0))} = \frac{v(x(x_0, t_0), z(x_0, t_0))}{|Q(x_0, t_0)|} \tag{6}$$

in 2D, where $v_m(x_0, t_0)$ is the time migration velocity, and

$$\frac{\partial}{\partial t_0}(t_0 \mathbf{V}_m^2(\mathbf{x}_0, t_0)) = v^2(\mathbf{x}(\mathbf{x}_0, t_0))(\mathbf{Q}^T(\mathbf{x}_0, t_0)\mathbf{Q}(\mathbf{x}_0, t_0))^{-1} \tag{7}$$

in 3D, where $\mathbf{V}_m^2$ is the matrix of the squares of the time migration velocities.

In [3], we used Eqs. (6) and (7) as a basis for our inversion techniques, i.e. for finding v and **Q** from the Dix velocity. These techniques required solving system (8) and (9) below and hence estimating the second derivatives of the unknown velocity. This led to the problems mentioned in the overview.

In the present work, we develop partial differential equations in the time-domain variables $(\mathbf{x}_0, t_0)$ connecting the geometrical spreading and the Dix velocities. In result, we avoid the need of estimating the second derivatives of the unknown velocity and end up with better working and more reliable methods.

3. PDE for Q in 2D

This section is a more complete version of our discussion in [6]. From now on, we denote the Dix velocities by f to avoid the subscript and to emphasize that f is defined as the ratio of the true velocity and the geometrical spreading Q rather than from the time migration velocities.

Suppose a set of image rays is propagating downwards from the surface. Suppose we are tracing these rays and computing the quantities Q and P along them. P is the conjugate quantity for Q: if Q is considered a generalized coordinate, then P is the corresponding generalized momentum. Along each ray, Q and P evolve according to [19,7,18]

$$\frac{dQ}{dt_0} = v^2 P, \tag{8}$$

$$\frac{dP}{dt_0} = -\frac{v_{qq}}{v}Q. \tag{9}$$

Here v is the velocity along the ray, and v_{qq} is the second derivative of the velocity in the direction normal to the ray. If the velocity is known, one can easily trace each ray independently and find Q and P. However, we are considering the case where the velocity is unknown and needs to be found. In the previous work [3] we found the velocity directly by solving Eqs. (8) and (9) and using Eq. (6). In this work, we are going to rewrite Eqs. (8) and (9) as a system of PDE's with dependent variables Q and P and independent variables x_0 and t_0 using Eq. (6) and the definition of Q.
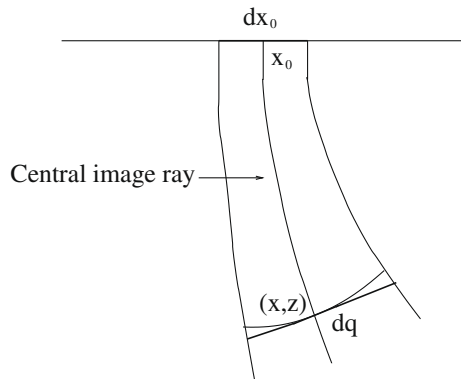

Fig. 2. Illustration for the definition of Q.

First we eliminate the velocity v in the system (8) and (9) using Eq. (6):

$$\frac{dQ}{dt_0} = (fQ)^2 P, \tag{10}$$

$$\frac{dP}{dt_0} = -\frac{(fQ)_{qq}}{f}. \tag{11}$$

We omit the absolute value around Q as we assume that we consider the time domain $\{(x_0, t_0)|x_{0min} \leqslant x_0 \leqslant x_{0max}, 0 \leqslant t_0 \leqslant t_{0max}\}$ to non-intersecting image rays. In other words, our time domain does not contain caustics. Next, we rewrite this system in the time coordinates (x_0, t_0). According to the chain rule,

$$\frac{d}{dq} = \frac{d}{dx_0}\frac{dx_0}{dq}. \tag{12}$$

By the definition of Q,

$$Q = \frac{dq}{dx_0}. \tag{13}$$

Hence,

$$\frac{d}{dq} = \frac{1}{Q}\frac{d}{dx_0}. \tag{14}$$

Applying this to system (10) and (11) we obtain the following system of PDE's:

$$Q_{t_0} = (fQ)^2 P, \tag{15}$$

$$P_{t_0} = -\frac{1}{fQ}\left(\frac{(fQ)_{x_0}}{Q}\right)_{x_0}. \tag{16}$$

Now let us recast system (15) and (16) to make its type more apparent and make it more suitable for discretization. For brevity, we will use notations t for t_0 and x for x_0. There should be no confusion since from now on, we work only in the time domain. Eq. (15) can be rewritten as

$$\frac{Q_t}{(fQ)^2} = P. \tag{17}$$

Differentiate this equation w.r.t. t and substitute into Eq. (16). Then we get

$$\left(\frac{Q_t}{(fQ)^2}\right)_t = -\frac{1}{fQ}\left(\frac{(FQ)_x}{Q}\right)_x, \tag{18}$$

and the initial conditions for this equation are

$$Q(x, 0) = 1, \quad Q_t(x, 0) = 0. \tag{19}$$

These follow from the initial conditions for the image rays traced downward the earth starting at the surface: $Q = 1, P = 0$.

Eq. (18) reveals the nature of both the sensitivity and the ill-posedness of the problem of seismic velocity estimation from time migration. First, its right-hand side contains the first and the second derivatives in x of $f(x, t)$. Hence, the time evolution of Q is explicitly governed not only by the input data $f(x, t)$ but also by their first two derivatives: this suggests a highly sensitive calculation, since accurate computation of these derivatives can be difficult. We also note that the left-hand side contains the first derivative in t of $f(x, t)$. At the same time, we also observe that Eq. (18) is a non-linear (quasilinear) second-order elliptic equation. At first glance, the geometry of the problem might suggest an underlying wave equation, since it is natural to think about the collection of the image rays as stemming from a flat wave that is propagating from the surface downward the earth. However, in reality there is no such wave. Instead, this is merely a device to think about the ordering inherent in constructing the solution from the top level downwards. In actuality, and as we shall see in detail below, we have in fact a Cauchy problem for an elliptic equation, which is well-known to be ill-posed in the sense that if we have two different initial conditions at $t = 0$, we cannot bound the difference between the corresponding solutions on the time interval $0 < t < \infty$.

These the explicit dependence of the first two derivatives and the ellipticity might seem to make solving this problem intractable. However, we argue that this is not so. First, in constructing a velocity model, we are mainly interested in the major and large features. Thus, we can smooth the input data to remove the small oscillations which are unimportant for the major features but may significantly change Q. Second, we do not need to compute the solution for a large time interval. Indeed, typical seismic velocities are between 1.5 and 5 km/s, while typical time intervals for which the seismic data are available (one-way time intervals) are less than 2 s. The lateral width of the interval from which seismic data are collected is of the order of 10 km, while the maximal depth up to which geophysicists can hope to obtain a seismic image from such data is between 3 and 5 km.

In the next section we will demonstrate that we can solve this Cauchy problem numerically. In Section 5 we will explain why we are able to do so.

4. 2D numerics

We build the velocity model in depth from the Dix velocities given in the time coordinates into two steps:

Step 1. Compute the geometrical spreading Q in the time-domain coordinates from the Dix velocity by solving equation (18). Then find $v(x_0, t_0)$ from Eq. (6).

Step 2. Convert the seismic velocity $v(x_0, t_0)$ in the time coordinates to the depth coordinates (x, z) using the time-to-depth conversion algorithm, which was presented by [3]. It is a fast and robust Dijkstra-like solver motivated by the Fast Marching method [21–24].

In this section, we present two numerical approaches for solving a Cauchy problem for Eq. (18) with initial conditions (19). One approach in a finite difference approach, inspired by the Lax–Friedrichs scheme. The second approach is a Chebychev spectral method. Our goal is to demonstrate that we are able to find a way to compute the solution of the Cauchy problem (18) and (19) despite the fact that we are dealing with a Cauchy problem for an elliptic equation. We will discuss the theoretical questions raised by this fact in Section 5.

4.1. A finite difference algorithm

We now present an algorithm to solve Eq. (18) numerically. Consider for a moment the Lax–Friedrichs method for the hyperbolic conservation laws of the form $u_t + [F(u)]_x = 0$ [15], namely

$$u_j^{n+1} = \frac{u_{j-1}^n + u_{j+1}^n}{2} - \frac{\Delta t}{2\Delta x}(F_{j+1}^n - F_{j-1}^n). \tag{20}$$

The Lax–Friedrichs method is a stable, total variation diminishing monotone scheme [16], which can be written in a conservation form for given flux [16], and guarantees that shock waves propagate with a correct speed.

Motivated by some of the smoothing properties of Lax–Friedrichs, we wish to develop a numerical scheme for System (15) and (16) with good stability properties. In a suggestive form, we view Eq. (18) as

$$g_t = -\alpha h_x \tag{21}$$

for $g = \frac{Q_t}{f^2 Q^2}, h = \frac{(fQ)_x}{Q}$ and $\alpha = \frac{1}{fQ}$ and take the idea of spatial averaging and symmetric central differencing from the Lax–Friedrichs scheme (20). To be sure, system (15) and (16) is not a system of conservation laws, and the motivation for using this sort of differencing structure should not be viewed as connected to a conservation form.

Note that

$$P \equiv \frac{Q_t}{f^2 Q^2} \equiv \frac{1}{f^2}\left(-\frac{1}{Q}\right)_t. \tag{22}$$

This suggests that, at each time step, we execute two steps. First, we use an approximation scheme for Eq. (16), followed by the trapezoidal rule for the approximation of Eq. (15):

$$P_j^{n+1} = \frac{P_{j+1}^n + P_{j-1}^n}{2} - \frac{\Delta t}{4\Delta x^2}\frac{1}{(fQ)_j^n}\left(\frac{(fQ)_{j+2}^n - (fQ)_j^n}{Q_{j+1}^n} - \frac{(fQ)_j^n - (fQ)_{j-2}^n}{Q_{j-1}^n}\right), \tag{23}$$

$$-\frac{1}{Q_j^{n+1}} = -\frac{1}{Q_j^n} + \frac{\Delta t}{2}\left((f_j^n)^2 P_j^n + (f_j^{n+1})^2 P_j^{n+1}\right). \tag{24}$$

We impose the following boundary conditions $Q_0^n = Q_1^n = Q_{nx-2}^n = Q_{nx-1}^n = 1$, $P_0^n = P_1^n = P_{nx-2}^n = P_{nx-1}^n = 0$ corresponding the straight boundary rays. We have also tried to use one-sided schemes at the boundaries but this did not make any significant difference in the numerical results.

We set the initial conditions $Q_j^0 = 1, P_j^0 = 0$ corresponding to the initial conditions for the image rays traced backward: $Q = 1, P = 0$.

We apply Schemes (23) and (24) to first compute P_j^{n+1} and then compute the quantity $Q(x, t) \equiv Q(x_0, t_0)$. Then we find the velocity in time coordinates using the formula $v(x_0, t_0) = f(x_0, t_0)Q(x_0, t_0)$ given by Eq. (6), and finally we apply the time-to-depth conversion algorithm introduced in [3] to compute the seismic velocity $v(x, z)$ in the depth coordinates from that in the time coordinates $v(x_0, t_0)$.

We tested this scheme on a number of numerical examples. The scheme is able to recover the seismic velocity from the Dix velocity successfully and more accurately than our previous numerical methods presented in [3].

In Fig. 3 we present a synthetic example with a Gaussian anomaly centered at 2 km in depth:

$$v(x,z) = 2 + 2e^{-0.15(x^2+(z-2)^2)}, \quad -10 \leqslant x_0 \leqslant 10, \ 0 \leqslant t \leqslant 1.5. \tag{25}$$

Dark blue and dark red colors correspond to the velocities of $v = 2$ and $v = 4$ km/s, respectively.

We have successfully computed this example on $nx \times nt$ meshes $100 \times 100, 200 \times 200, 500 \times 500$ and 1000×1800.

In Fig. 4 we present another synthetic example with a narrower Gaussian anomaly centered at 2 km in depth:

$$v(x,z) = 2 + 2e^{-0.5(x^2+(z-2)^2)}, \quad -5 \leqslant x_0 \leqslant 5, \ 0 \leqslant t \leqslant 1. \tag{26}$$

Dark blue and dark red colors correspond to the velocities of $v = 2$ and $v = 4$ km/s, respectively. We computed the velocity almost up to the caustics, and used 500×1200 $nx \times nt$ mesh. The balance between the space and time steps was chosen such that we do not add too much smoothing due to a large space step while still suppressing the high harmonics (see Section 5.5) due to a large time step.

In Fig. 5 we present one more synthetic example with an asymmetric Gaussian anomaly. Dark blue and dark red colors correspond to the velocities of $v = 2$ and $v = 3.54$ km/s, respectively. Here we used $500 \times 1200 nx \times nt$ mesh.

We remark that we found Schemes (23) and (24) after experimenting with some other schemes (Schemes (55), (56), (58) and (59) below). We will explain our success with Schemes (23) and (24) and failure with the other two schemes in Section 5.5.

Next, we have tried to apply Schemes (23) and (24) to field data examples with severe lateral inhomogeneity. However, despite the fact that input data $f(x,t)$ (the Dix velocities found from the time-migrated velocities) were rather smooth and bounded by $1.5 < f(x,t) < 5$ km/s, our computed Q started to blow up after about 1 km in depth. An immediate question is to analyze whether this is a numerical effect or if in fact the exact solution of Eq. (18) with the given $f(x,t)$ indeed blows up in finite time. We point out that the governing function $f(x,t)$ determined from the time migration is not only inexact but also it may be qualitatively different from the exact $f(x,t) = \frac{x(x,t)}{|Q(x,t)|}$. Indeed, the experimental time migration velocities are smooth

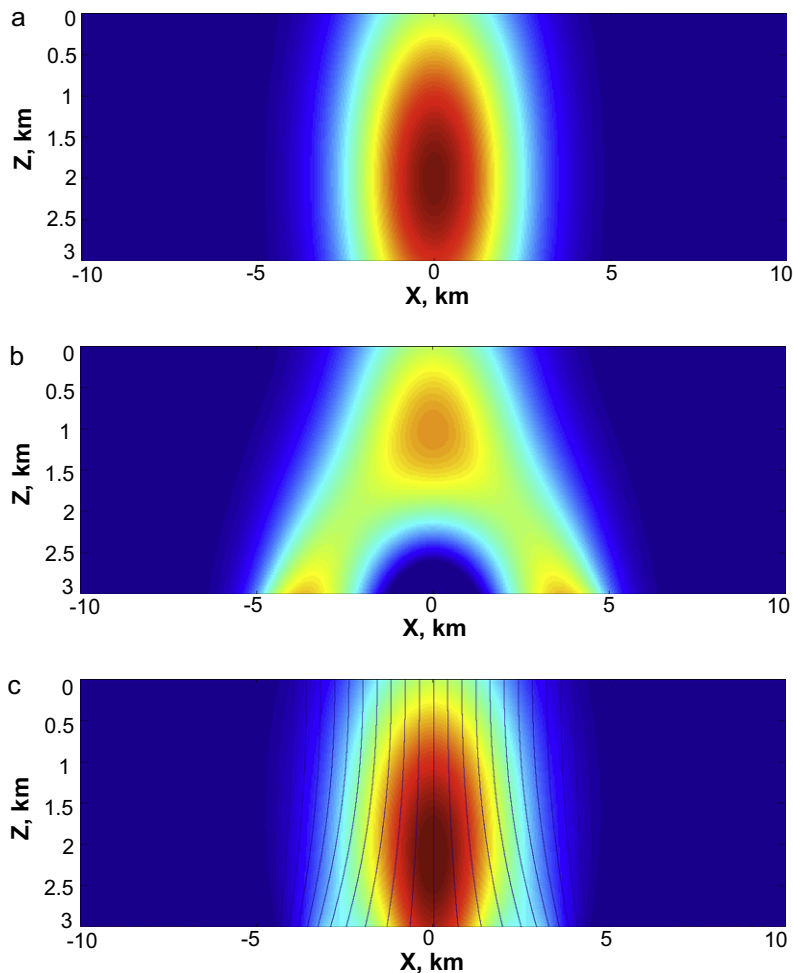**Fig. 3.** (a): The exact velocity; (b): the Dix velocity converted to depth; and (c): the found velocity and the image rays. Dark red (center): $v = 4$ km/s; dark blue (outer edges): $v = 2$ km/s. (For interpretation of the references to colour in this figure legend, the reader is referred to the web version of this article.)
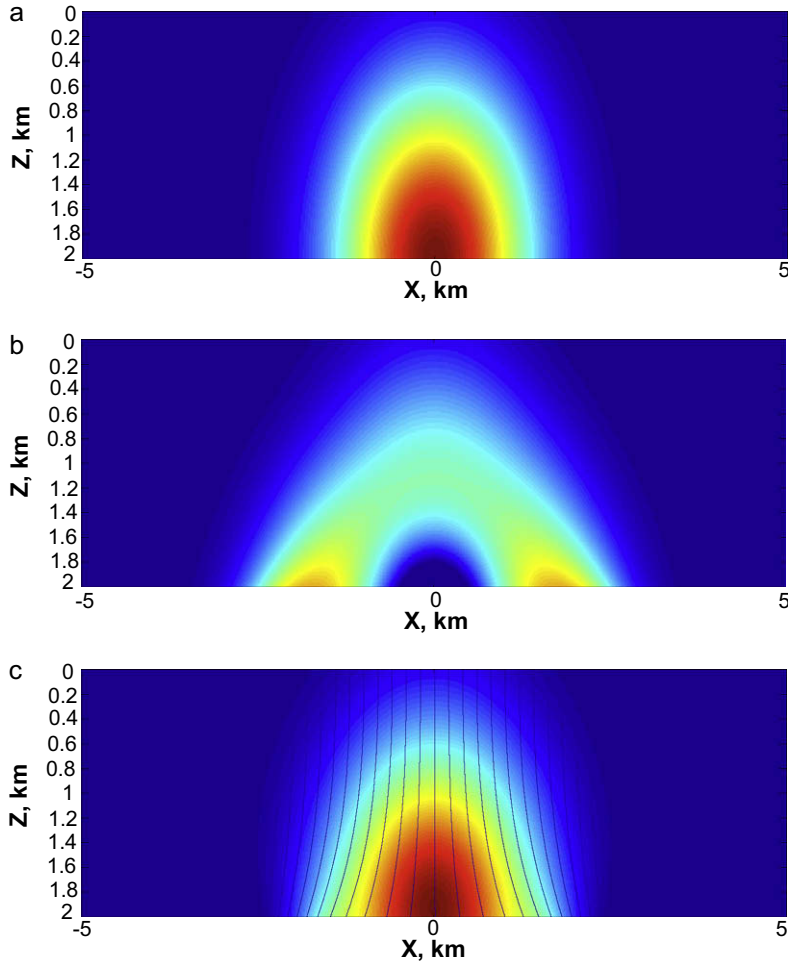
Fig. 4. (a): The exact velocity; (b): the Dix velocity converted to depth; and (c): the found velocity and the image rays. Dark red (center): $v = 4$ km/s; dark blue (outer edges): $v = 2$ km/s. (For interpretation of the references to colour in this figure legend, the reader is referred to the web version of this article.)

and bounded no matter how complex the seismic velocity distribution is. Mathematically, $f(x, t)$ must blow up as the image rays cross, but the time migration velocities are never chosen to have infinite derivatives. Hence, the following problem arises. Suppose $f(x, t)$ is a smooth and bounded function $0 < m \leqslant f(x, t) \leqslant M$. Is it possible that the solution of Eq. (18) with initial conditions $Q(x, 0) = 1, Q_t(x, 0) = 0$ blows up in a finite time? We will address this question in Section 5.4.

4.2. Spectral Chebyshev method

We also tried to apply a Chebyshev spectral method [1]. We used cubic splines to find the input data at N Chebyshev points. We compute the Chebyshev coefficients and the coefficients of the derivatives in the right-hand side of Eq. (18). Then we use a smaller number m of the coefficients for function evaluation. We need to do such Chebyshev differentiation twice. Finally we perform the time step using the third-order Adams–Bashforth method [1], which is

$$u^{n+1} = u^n + \Delta t \left(\frac{23}{12} F(u^n, x, t^n) - \frac{4}{3} F(u^{n-1}, x, t^{n-1}) + \frac{5}{12} F(u^{n-2}, x, t^{n-2}) \right).$$

(27)

We used $N = 100$ and $m = 20$. Increase of the number of coefficients for function evaluation m leads to rapidly developing oscillations. Decrease of m leads to smearing and lack of correction of the velocity. This method allows us to restore the seismic velocity for smaller depths than the finite difference method on the same synthetic data examples. The examples in Figs. 6 and 7 are the same as the examples in Figs. 3 and 5 for the finite difference method. With the Chebyshev method we were able to restore the velocity up to 2 km in depth in both cases versus 3 km and 2.8 km with the finite difference method.

This method provides an alternative to finite differences to solve Eq. (18): it works by using series truncation for regularization rather than small finite difference error terms. Moreover, this method allows us to penetrate deeper into the earth, sacrificing some exactness, i.e. reducing the number of polynomials m used for the function evaluation.
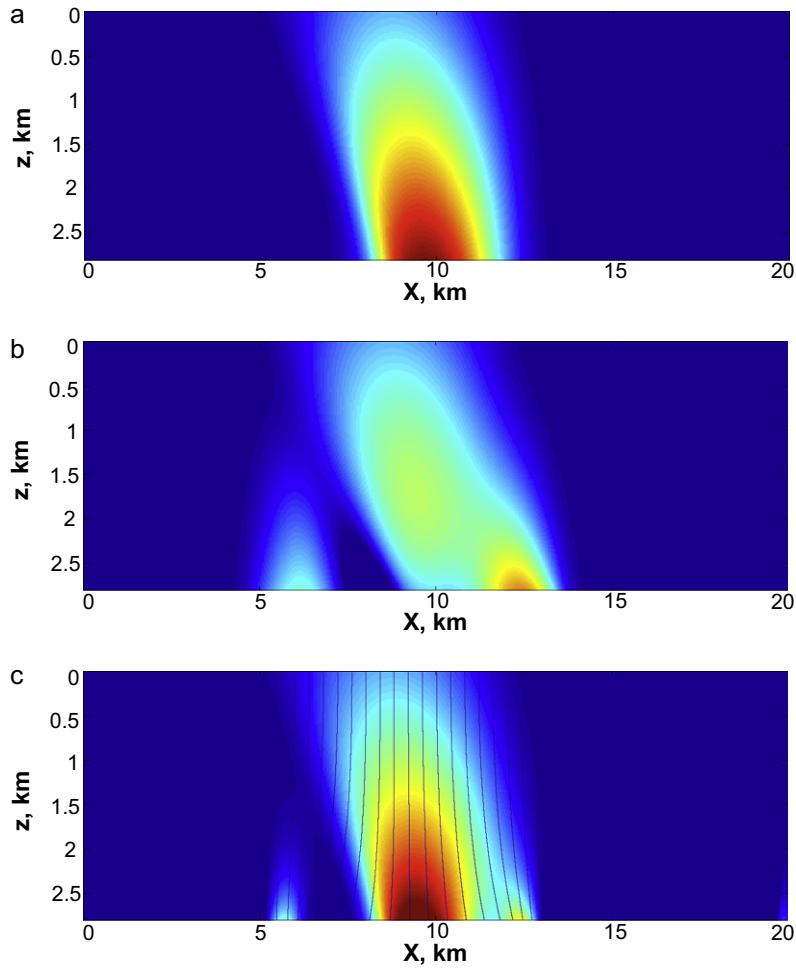
Fig. 5. (a): The exact velocity; (b): the Dix velocity converted to depth; and (c): the found velocity and the image rays. Dark red (center): $v = 3.54$ km/s; dark blue (outer edges): $v = 2$ km/s. (For interpretation of the references to colour in this figure legend, the reader is referred to the web version of this article.)

5. Cauchy problem for the elliptic PDE for Q

5.1. Ellipticity of the Equation for Q

For simplification of the PDE for Q, we will work with its negative reciprocal

$$y = -\frac{1}{Q}$$

(28)

instead. For y, our PDE becomes the following:

$$\left(\frac{y_t}{f^2}\right)_t = \frac{y}{f}\left(\left(\frac{f}{y}\right)_x y\right)_x.$$

(29)

The initial conditions for y are the following:

$$y(x,0) = -1, \quad y_t(x,0) = 0.$$

(30)

First note that Q is an increasing function of y s.t. Q tends to $+\infty$ as $y \to 0$, and Q tends to zero as $y \to -\infty$ (see Fig. 8). Opening the parentheses in Eq. (29) we get:

$$\frac{y_{tt}}{f^2} - 2\frac{y_t f_t}{f^3} = y\frac{f_{xx}}{f} - y_x\frac{f_x}{f} - y_{xx} + \frac{y_x^2}{y}.$$

(31)

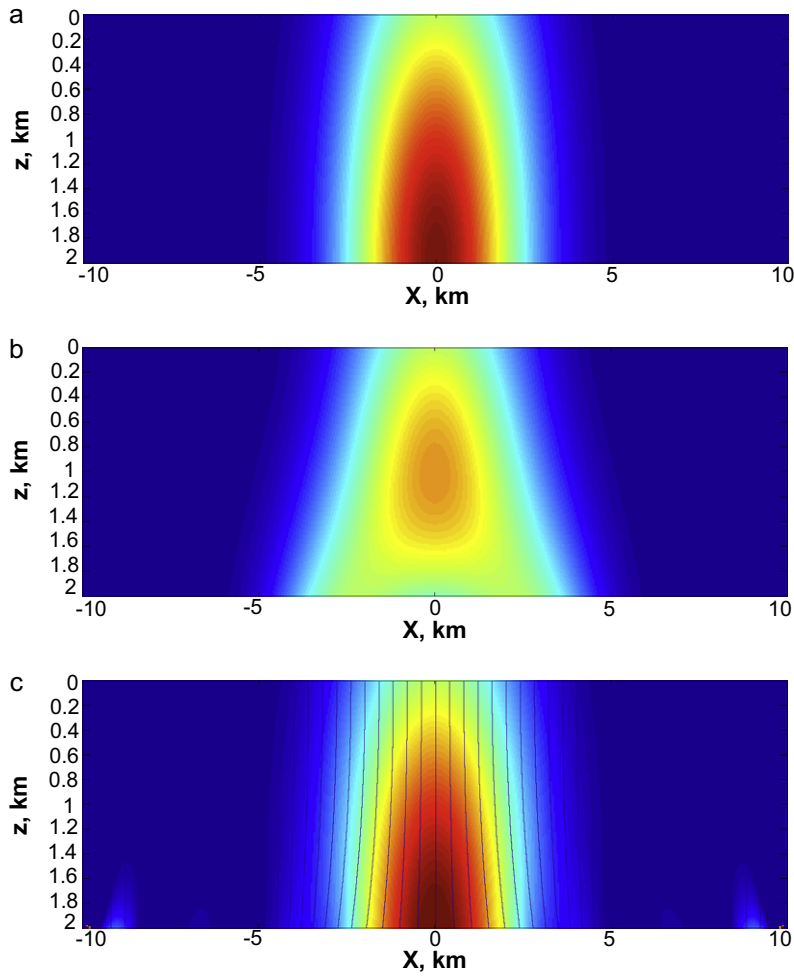From this form, it is apparent that the PDE is elliptic.

Fig. 6. (a): The exact velocity; (b): the Dix velocity converted to depth; and (c): the found velocity and the image rays. Dark red (center): $v = 4$ km/s; dark blue (outer edges): $v = 2$ km/s. (For interpretation of the references to colour in this figure legend, the reader is referred to the web version of this article.)

5.2. Ill-posedness of elliptic initial value problems

We start our discussion by considering a variant of the famous Hadamard's example of an ill-posed problem: a Cauchy problem for the familiar Laplace's equation on a finite interval:

$$y_{tt} = -y_{xx}, \quad 0 \leqslant x \leqslant 1, \; y(0,t) = y(1,t) = 1. \tag{32}$$

If the initial conditions are

$$y(x,0) = 1, \quad y_t(x,0) = 0, \tag{33}$$

this problem has a unique solution $y(x,t) = 1$. Let us perturb the initial conditions and make them

$$\tilde{y}(x,0) = 1 + e^{-\sqrt{\pi n}} \sin \pi n x, \quad \tilde{y}_t(x,0) = 0. \tag{34}$$

Any Sobolev norm of this perturbation tends to zero as $n \to \infty$. Hence by choosing n to be sufficiently large we can make the norm of the perturbation of the initial condition arbitrarily close to zero. Then the solution of the perturbed problem is

$$\tilde{y}(x,t) = 1 + e^{-\sqrt{\pi n}} \sin \pi n x \cosh \pi n t. \tag{35}$$

For any fixed $t > 0$ any Sobolev norm of $(\tilde{y}(x,t) - 1)$ goes to infinity as $n \to \infty$. Thus this problem does not depend continuously on the data, and hence is not well-posed.

However, Klibanov and Santosa in [13] showed that the original Laplace equation can be replaced with a different equation with a small parameter ϵ such that the Cauchy problem for the modified equation is well-posed and its solution
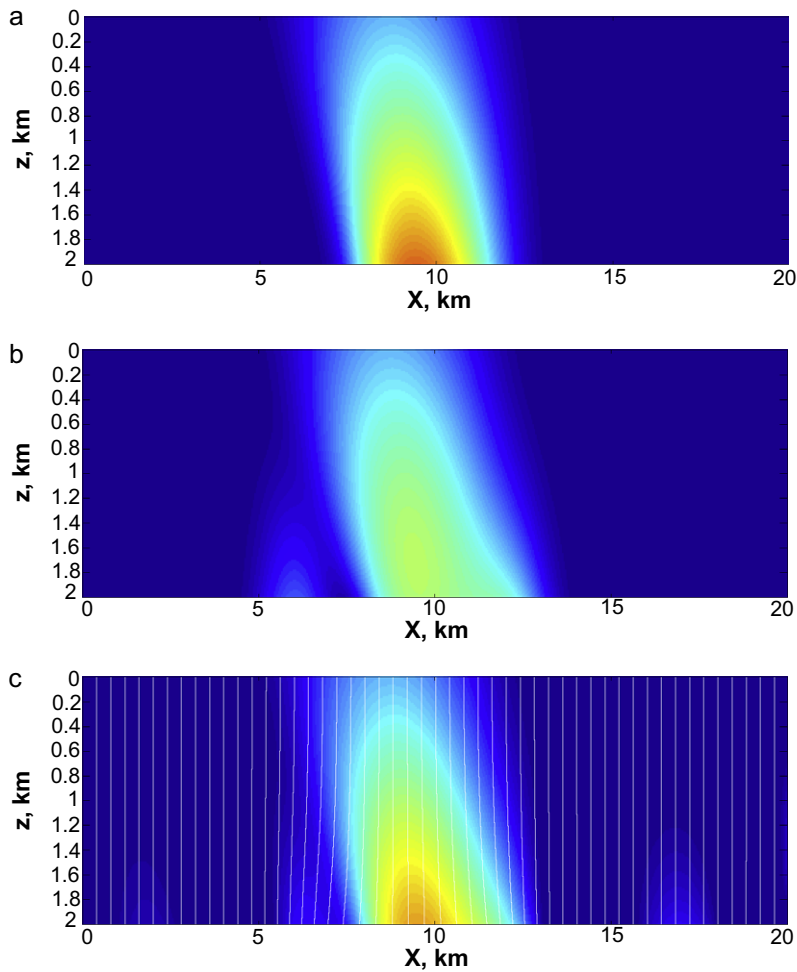
Fig. 7. (a): The exact velocity; (b): the Dix velocity converted to depth; (c): the found velocity and the image rays. Dark red (center): $v = 3.54$ km/s; dark blue (outer edges): $v = 2$ km/s. (For interpretation of the references to colour in this figure legend, the reader is referred to the web version of this article.)
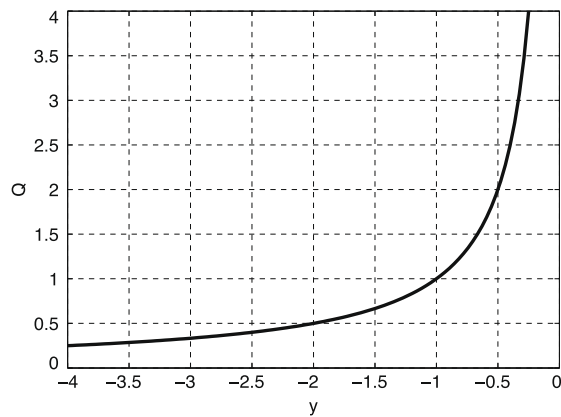

Fig. 8. The relation between Q and its negative reciprocal y.

converges to the solution of the original Cauchy problem as $\epsilon \to 0$ in some bounded specified domain. Their argument relies on the linearity of Laplace's equation and uses the theory of linear functional spaces. Our PDE is non-linear and we cannot use similar tools.

5.3. Sensitivity and stability of our particular PDE

Now let us return to our equation. We have demonstrated that we are able to compute a solution stably. We claim that the reasons for this are the following:

1. We have (i) very specific initial conditions which are the only physically relevant conditions $Q(x, 0) = -1/y = 1$, $Q_t(x, 0) = y_t(x, 0) = 0$, and (ii) a very specific governing function (the Dix velocity) $f(x, t)$ corresponding to some bounded seismic velocity $v(x, t)$. If the governing function $f(x, t)$ could be known exactly, then these initial conditions are such that the exact solution $Q(x, t) = -1/y(x, t)$ is finite and non-zero if $f(x, t)$ is finite.
2. Of course, the governing function $f(x, t)$ is never known exactly. While initial conditions are known exactly, their representation has error on the order of machine precision. More importantly, our numerical scheme supports only a limited number of harmonics, from 0 up to $\frac{\pi}{\Delta x}$, and additionally suppresses the amplitude growth of the high harmonics which it supports. We note, of course, that it does not suppress the amplitude growth of the low harmonics. Since we need to compute the solution only for a small interval of time, these low harmonics do not grow significantly during that period. For example, typically, the velocity is of the order of a few kilometers per second, while the input data $f(x, t)$ are available only for less than 2 s. (We refer to the one-way maximal travel time.)

5.4. Solution in the case of non-special initial data or a non-special governing function

We now examine in some more detail the nature of our elliptic initial value problem.

1. In the special case of $f(x, t) \equiv 1$, with our given initial conditions given by $y(x, 0) = -1, y_t(x, 0) = 0$ (Eq. (30)), it is easy to see that a solution is given by $y = -1$. However, we will first show by example that for other (non-physical) initial conditions, the analytical solution for Eq. (29) can become zero (i.e. Q becomes $+\infty$) in a finite time, even if $f(x, t) \equiv 1$;
2. Next, we will show that the analytical solution for Eq. (29) with the physical initial condition (30), can blow up (become zero in finite time), even when $f(x, t)$ is a bounded analytic function with all bounded derivatives.

Since $v(x, t) = f(x, t)Q(x, t)$ and we assume that $f(x, t)$ is positive and finite, the zero Q corresponds to zero v and infinite Q corresponds to infinite v for a finite f. Both of these are not physical.

Claim 1. *Suppose $f(x, t) = 1$ in Eq. (29). We consider the following initial and boundary value problem:*

$$y_{tt} = -y_{xx} + \frac{y_x^2}{y}, \quad a \leqslant x \leqslant b, \tag{36}$$

$$y(x, 0) = \alpha(x), \quad y_t(x, 0) = 0, \tag{37}$$

$$y(a, t) = y(b, t) = -1. \tag{38}$$

Let $\alpha(x)$ be a smooth analytic function such that

1. $-M \leqslant \alpha \leqslant -m < 0, \ \alpha(a) = \alpha(b) = -1$,
2. α has an absolute maximum at a point $x_0 \in (a, b) \ \alpha_{xx}(x_0) < 0$, and
3. $\alpha_{xx}(a) = \alpha_{xx}(b) = 0$.

Then the solution to the problem (36)–(38) becomes zero or $-\infty$ in a finite time. This corresponds to Q becoming infinitely large or zero, respectively.

Proof. Let τ be an infinitesimally small positive time. Then at $t = \tau$

$$y(x, \tau) = \alpha(x) + (-\alpha_{xx}) \frac{\tau^2}{2} + \frac{\alpha_x^2}{\alpha} \frac{\tau^2}{2}. \tag{39}$$

We claim that $y_{tt}(x_0, t)$ is positive for $0 < t \leqslant \tau$ as $-\alpha_{xx}(x_0)$ is positive, and $\alpha_x(x_0)$ is zero. Taking into account that $y_t(x, 0) = 0$ we conclude that $y_t(x_0, \tau) > 0$.

Now we consider $y(x_{max}(t))$, where $x_{max}(t)$ is the point of the absolute maximum of $y(x, t)$ at time t. We first note that the absolute maximum is reached at an inner point of the interval (a, b) at any $t > 0$ while the solution exists. Indeed, with y set to -1 at the endpoints, the absolute maximum is reached at an inner point according to Eq. (39) for $0 < t \leqslant \tau$. Moreover, y_{tt} is non-negative at any local maximum in (a, b) since $y_{tt} = -y_{xx}$ at a local maximum. Hence y_t is non-decreasing at any local maximum and y is growing with a non-negative acceleration at any local maximum. One of these local maximums must be the absolute maximum. Furthermore, the function $x_{max}(t)$ need not be constant and nor continuous. If, at some time $t_1, y(x_1, t_1) = y(x_2, t_1)$ and $y(x_1, t) > y(x_2, t)$ for $t < t_1$ and $y(x_1, t) < y(x_2, t)$ for $t > t_1$ in some neighborhood of t_1, then $y_t(x_1, t_1) \leqslant y_t(x_2, t_1)$. Therefore, $y_t(x_{max}(t))$ is non-decreasing. Thus, $y_t(x_{max}) \geqslant y_t(x_0, \tau) > 0$ which means that the absolute maximum of y grows at least linearly and hence must reach zero in finite time unless y becomes $-\infty$ at some point before that. This completes the proof. $\square$

Note that no matter how little $\alpha(x)$ in Claim 1 differs from -1 and all its derivatives differ from 0, y still must either become zero or infinite in a finite time. If α is -1 then the only solution of problem (36)–(38) is $y(x,t) = -1$. Hence the solution is unstable w.r.t. small perturbations of the initial data.

Claim 2. *Consider the following initial and boundary value problem for* Eq. (31):

$$y(x,0) = -1, \quad y_t(x,0) = 0 \tag{40}$$
$$y(a,t) = y(b,t) = -1. \tag{41}$$

Suppose the function f in Eq. (31) is analytic and satisfies the following conditions:

1. $f(x,t)$ *is independent of t;*
2. $f(x)$ *is bounded: $0 < m \leqslant f(x) \leqslant M$;*
3. $f_{xx} \leqslant 0$ *on (a,b) and $f_{xx}(a) = f_{xx}(b) = 0$.*
4. f *and ff_{xx} reach their absolute maximums at the same point $x_0 \in (a,b)$ and $f_{xx}(x_0) < 0$.*

Then the solution to the problem (31), (40), *and* (41) *becomes zero or $-\infty$ in a finite time. This corresponds to Q becoming infinitely large or zero respectively.*

Note that there is a large class of functions satisfying the conditions for function $f(x)$ in Claim 9, e.g. $f(x) = 2 + \cos x$ on the interval $\left[-\frac{\pi}{2}, \frac{\pi}{2}\right]$, or of $f(x) = 1 + e^{-\frac{x^2}{2}}$ on the interval $[-1, 1]$.

Proof. First, let us rewrite Eq. (31) taking into account that $f(x,t) = f(x)$:

$$y_{tt} = ff_{xx}y - ff_x y_x - f^2 y_{xx} + f^2 \frac{y_x^2}{y}. \tag{42}$$

Let τ be an infinitesimally small positive time. Then at $t = \tau$

$$y(x,\tau) = -1 + (-ff_{xx})\frac{\tau^2}{2}. \tag{43}$$

Notice that $y_{tt}(x_0)$ is positive for $0 < t \leqslant \tau$ as ff_{xx} is negative and the other terms in Eq. (42) are zero due to the initial condition $y(x,0) = -1$. Taking into account that $y_t(x,0) = 0$ we conclude that $y_t(x_0, \tau) > 0$.

We point out that y_{tt} is non-negative at any local maximum, since

$$y_{tt} = yff_{xx} - y_{xx},$$

where $y < 0, ff_{xx} \leqslant 0$ and $y_{xx} \leqslant 0$. The rest of the proof closely repeats the one of Claim 1. $\square$

Therefore, if the input Dix velocity is not exactly $\frac{v(x,t)}{Q(x,t)}$, the exact solution of Eq. (18) might blow up in a finite time under our given governing function $f(x,t)$.

Remark. It worth mentioning that the equation

$$y_{tt} = -y_{xx} + \frac{y_x^2}{y} \tag{44}$$

can be solved by the separation of variables method. This method leads to solutions of the form

$$y(x,t) = (A\cosh \omega t + B\sinh \omega t)e^{-\frac{\omega^2 x^2}{2} + \mu x} \tag{45}$$

and

$$y(x,t) = (A\cos \omega t + B\sin \omega t)e^{\frac{\omega^2 x^2}{2} + \mu x}, \tag{46}$$

where A, B, ω and μ are arbitrary constants. However, these solutions are not particularly relevant to our problem. If we consider an initial value problem on $\mathbb{R} \times [0, +\infty)$, then these solutions satisfy either unbounded or tending to zero initial conditions, which is non-physical. If we consider an initial and boundary value problem on a bounded space interval, then these solutions satisfy either unbounded or tending to zero boundary conditions which is again non-physical. While any constant times a solution to Eq. (44) is itself a solution, due to non-linearity, the sum of solutions of Eq. (44) is not a solution in general.

5.5. Inexact input and initial conditions

Next, we further analyze the effect of perturbations and the growth of oscillations under our numerical scheme. We begin with a perturbation analysis, and then study how our numerical schemes behave on a perturbation equation.

5.5.1. Perturbation analysis

Suppose $f(x,t)$ is perfect input data corresponding to some smooth seismic velocity $v(x,t)$, $0 < m \leqslant v(x,t) \leqslant M$. Let $y(x,t)$ be the exact solution of Eq. (29) with the initial conditions (30). Let $f(x,t) + \delta f(x,t)$ be the inexact (perturbed) input data, and $y(x,t) + \delta y(x,t)$ be the exact solution of Eq. (29) with the inexact input data $f + \delta f$ and the initial condition (30). Plugging $y + \delta y$ and $f + \delta f$ into Eq. (31) and linearizing around the exact input $f(x,t)$ and the exact solution of the non-perturbed problem $y(x,t)$, we obtain

$$\frac{y_{tt}}{f^2} - 2\frac{y_{tt}\delta f}{f^3} + \frac{\delta y_{tt}}{f^2} - 2\frac{y_t f_t}{f^3} - 2\frac{\delta y_t f_t}{f^3} - 2\frac{y_t \delta f_t}{f^3} + 6\frac{y_t f_t \delta f_t}{f^4}$$
$$= \frac{f_{xx}}{f}y + \frac{\delta f_{xx}}{f}y + \frac{f_{xx}}{f}\delta y - \frac{f_{xx}}{f^2}y\delta f - \frac{f_x}{f}y_x - \frac{\delta f}{f}y_x - \frac{f_x}{f}\delta y + \frac{f_x}{f^2}y_x\delta f - y_{xx} - \delta y_{xx} + \frac{y_x^2}{y} + 2\frac{y_x\delta y_x}{y} - \frac{y_x^2}{y^2}\delta y.$$

Cancelling the terms from Eq. (31) we obtain the following equation for δy:

$$\frac{\delta y_{tt}}{f^2} - 2\frac{\delta y_t f_t}{f^3} - \frac{f_{xx}}{f}\delta y + \frac{f_x}{f}\delta y_x + \delta y_{xx} + \delta y_x\left(\frac{y_x^2}{y^2} - 2\frac{y_x}{y}\right) = \mathcal{F}, \tag{47}$$

where $\mathcal{F} = \mathcal{F}(y, y_x, y_t, y_{tt}, f, f_x, f_x x, f_t, \delta f, \delta f_x, \delta f_{xx}, \delta f_t, \delta f_{tt})$. We immediately observe that Eq. (47) is a linear elliptic equation with growing harmonics.

5.5.2. Our scheme and the associated modified equations

We now investigate how our numerical scheme for Eq. (29) responds due to truncation errors. We focus on Schemes (23) and (24). First, we rewrite Scheme (23) and (24) in terms of y:

$$P_j^{n+1} = \frac{P_{j-1}^n + P_{j+1}^n}{2} - \frac{\Delta t}{4\Delta x^2}\frac{y}{f}\left((v_{j+2}^n - v_j^n)y_{j+1} - (v_j^n - v_{j-2}^n)y_{j-1}\right), \tag{48}$$

$$y_j^{n+1} = y_j^n + \frac{\Delta t}{2}\left((f^2)_j^n P_j^n + (f^2)_j^{n+1}P_j^n\right), \tag{49}$$

where $P \equiv \frac{y_t}{f^2}$ and $v \equiv -\frac{f}{y}$. Applying Taylor expansion to the terms of the first equation, we obtain the following modified equation for y which Eq. (48) approximates more exactly:

$$\left(\frac{y_t}{f^2}\right)_t = \frac{y}{f}\left(\left(\frac{f}{y}\right)_x y\right)_x + \frac{\Delta x^2}{2\Delta t}\left(\frac{y_t}{f^2}\right)_{xx} - \frac{\Delta t}{2}\left(\frac{y_t}{f^2}\right)_{tt} - \Delta x^2\frac{y}{f}\left(\frac{1}{3}v_{xxxx}y + \frac{1}{3}v_{xxx}y_x - \frac{1}{2}v_{xx}y_{xx} + \frac{1}{6}v_x y_{xxx}\right). \tag{50}$$

Let us apply the modified equation Eq. (50) to the perturbed problem. For simplicity, we consider the case where $f(x,t) = 1$, hence $y(x,t) = -1$. In this case,

$$v = -\frac{1}{y}, \quad v_x = \frac{\delta y_x}{y^2}, \quad v_{xx} = \frac{\delta y_{xx}}{y^2} + \cdots, \quad v_{xxx} = \frac{\delta y_{xxx}}{y^2} + \cdots, \quad v_{xxxx} = \frac{\delta y_{xxxx}}{y^2} + \cdots,$$

where we ignore the second and higher order terms. Linearizing the modified equation around $f = 1$ and $y = -1$ we obtain:

$$\delta y_{tt} + \delta y_{xx} - \frac{\Delta x^2}{2\Delta t}\delta y_{txx} + \frac{\Delta t^2}{2}\delta y_{ttt} + \frac{\Delta x^2}{3}\delta y_{xxxx} = \mathcal{F}, \tag{51}$$

where $\mathcal{F} = \mathcal{F}(\delta f, \delta f_x, \delta f_{xx}, \delta f_t, \delta f_{tt})$. Let $a(k,t)$ be the Fourier transform of $y(x,t)$ in x. Then a satisfies the following equation:

$$\frac{\Delta t^2}{2}a_{ttt} + a_{tt} + \frac{\Delta x^2}{2\Delta t}k^2 a_t + \left(\frac{\Delta x^2}{3}k^4 - k^2\right)a = \widehat{\mathcal{F}}. \tag{52}$$

Note that the linearized original equation Eq. (47) in the case where $f(x,t) = 1$ and hence $y(x,t) = -1$ becomes:

$$\delta y_{tt} + \delta y_{xx} = \mathcal{F}. \tag{53}$$

The corresponding equation for the amplitudes of the Fourier harmonics is

$$a_{tt} - k^2 a = \widehat{\mathcal{F}}. \tag{54}$$

The real parts of the eigenroots of Eq. (52) as functions of the harmonic number k are shown in Fig. 9(a). (Such kind of analysis can be found in [17].) Characters ×, +, ∘ and ◇ correspond to $\Delta x/\Delta t = 1$, $\Delta x/\Delta t = 2$, $\Delta x/\Delta t = 5$ and $\Delta x/\Delta t = 10$, respectively. For reference, the eigenroots of Eq. (54) are also plotted there with characters ∗.

First, we note that the fact that the plots for various ratios $\Delta x/\Delta t$ are tangent to the lines corresponding to the exact equation indicates the consistency of Schemes (48) and (49). The plots in Fig. 9(a) show that we can find such ratio $\Delta x/\Delta t$ for the Schemes (48) and (49) that the growth of the higher harmonics is suppressed. Although we cannot suppress the growth of the lower harmonics (which is a necessary condition for consistency), we need only compute the solution for a rather short interval of time, and this period is short enough that the lower harmonics do not grow significantly.

5.5.3. Alternative schemes

We now investigate two alternative schemes, and show why they are not appropriate for our problem. To begin, suppose we remove the Lax–Friedrichs averaging from Eq. (48):

$$P_j^{n+1} = P_j^n - \frac{\Delta t}{4\Delta x^2}\frac{y}{f}((v_{j+2}^n - v_j^n)y_{j+1}^n - (v_j^n - v_{j-2}^n)y_{j-1}^n),$$

(55)

$$y_j^{n+1} = y_j^n + \frac{\Delta t}{2}\left((f^2)_j^n P_j^n + (f^2)_j^{n+1}P_j^n\right).$$

(56)

Then the corresponding modified and linearized modified equations miss the term $\frac{\Delta x^2}{2\Delta t}(\frac{y_t}{f^2})_{xx}$, and the equation for the corresponding equation for the amplitudes of the Fourier harmonics becomes
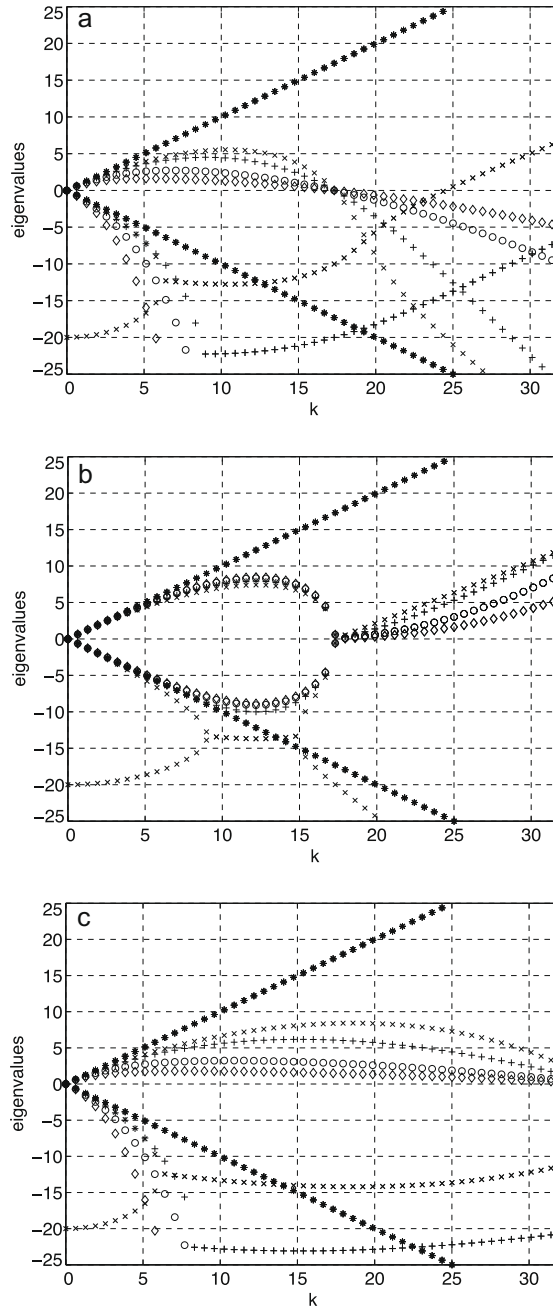

Fig. 9. The root diagrams for (a): the "Lax–Friedrichs" averaging scheme with 5-point stencil in space; (b): the same scheme without the "Lax–Friedrichs" averaging; and (c): the "Lax–Friedrichs" averaging scheme with 3-point stencil in space.

$$\frac{\Delta t^2}{2}a_{ttt} + a_{tt} + \left(\frac{\Delta x^2}{3}k^4 - k^2\right)a = \widehat{\mathcal{F}}.$$　(57)

The real parts of the eigenroots of Eq. (57) as functions of the harmonic number k are shown in Fig. 9(b). Again, characters $\times$, $+$, $\circ$ and $\diamond$ correspond to $\Delta x/\Delta t = 1, \Delta x/\Delta t = 2, \Delta x/\Delta t = 5$ and $\Delta x/\Delta t = 10$, respectively. Characters $*$ correspond to the eigenroots of Eq. (54) as before.

We see that the absence of the Lax–Friedrichs averaging leads to the growth of the high harmonics.

As yet another alternative, suppose now that we keep our Lax–Friedrichs averaging, but replace the 5-point stencil in space with a 3-point stencil in space in Eq. (48). We remark that the 3-point stencil leads to a smaller local truncation error than the 5-point stencil.

$$P_j^{n+1} = \frac{P_{j-1}^n + P_{j+1}^n}{2} - \frac{2\Delta t}{\Delta x^2}\frac{y}{f}((v_{j+1}^n - v_j^n)(y_{j+1}^n + y_j^n) - (v_j^n - v_{j-1}^n)(y_j^n + y_{j-1}^n)),$$　(58)

$$y_j^{n+1} = y_j^n + \frac{\Delta t}{2}\left((f^2)_j^n P_j^n + (f^2)_j^{n+1}P_j^n\right).$$　(59)

Then the corresponding equation for the amplitudes for the Fourier harmonics would be

$$\frac{\Delta t^2}{2}a_{ttt} + a_{tt} + \frac{\Delta x^2}{2\Delta t}k^2 a_t + \left(\frac{\Delta x^2}{12}k^4 - k^2\right)a = \widehat{\mathcal{F}}.$$　(60)

The real parts of the eigenroots of Eq. (57) as functions of the harmonic number k are shown in Fig. 9(c). Comparing figures (a) and (c) we see that Schemes (58) and (59) with the 3-point stencil in space suppresses the growth of all of the harmonics less than Schemes (48) and (49) with the 5-point in space.

To summarize Fig. 9 illustrates why we are able to restore the seismic velocity from the Dix velocity using scheme (48) and (49). The application of Schemes (55), (56), (58), and (59) on meshes finer than 100×100 leads to the highest spatial frequency $k = \pi/\Delta x$ oscillations.

Thus we have shown that our Schemes (48) and (49) is able to suppress the growth of the higher harmonics and hence can be used for computing the seismic velocity from the Dix velocity for a finite and small enough interval of time. It also seems that the other two Schemes (55), (56), (58), and (59) are worse than Schemes (48) and (49).

6. Marmousi example

In this section, we demonstrate an application of our method to the Marmousi synthetic data [28]. The prestack time-migrated image and the corresponding time migration velocity are shown in Fig. 10 and were generated by velocity continuation [9]. The Dix velocity computed from the time migration velocities and converted to depth by simple vertical stretching is shown in Fig. 11(a). The seismic velocity estimated from the Dix velocities with our Chebyshev method (using $N_{coef} = 500$ and $N_{eval} = 10$) and converted to depth using our time-to-depth conversion algorithm is shown in Fig. 11(b). We did not attempt to resolve the velocity below 1500 m, because, at larger depths, the image rays cross, and the time migration approach loses its validity. The prestack depth migrated images with Dix velocities and our velocities are shown in Fig. 12(a) and (b), respectively. The image obtained with our method appears to have more continuous reflectors. As a validation comparison, Fig. 13 shows angle-domain common-image point gathers [20] at 4000 m using the Dix velocity and the estimated velocity. The evident curvature of the events below 1000 m in depth gets removed as the events get properly positioned.
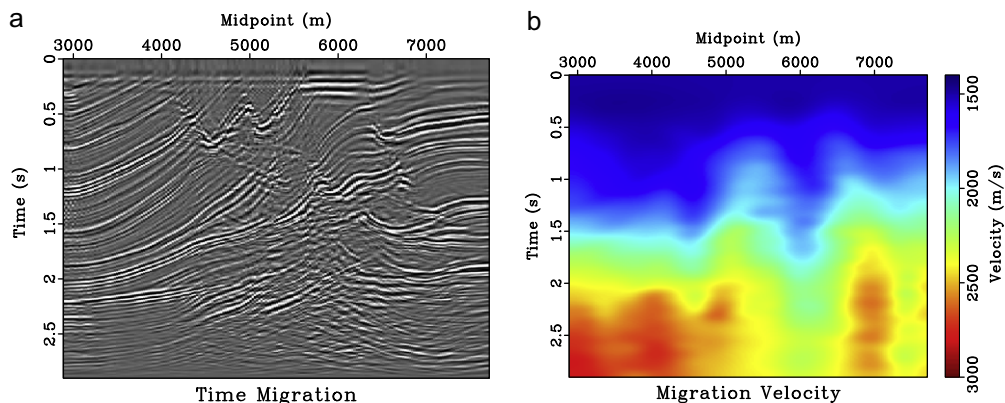

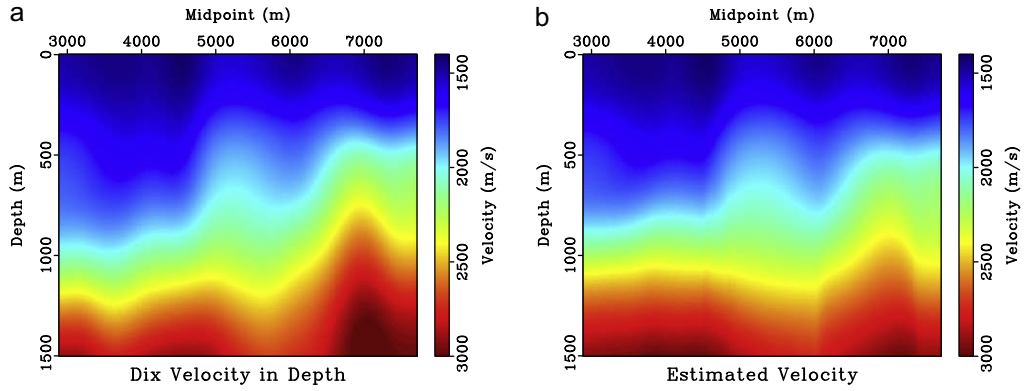**Fig. 10.** Time migrated image (a) and migration velocity (b).

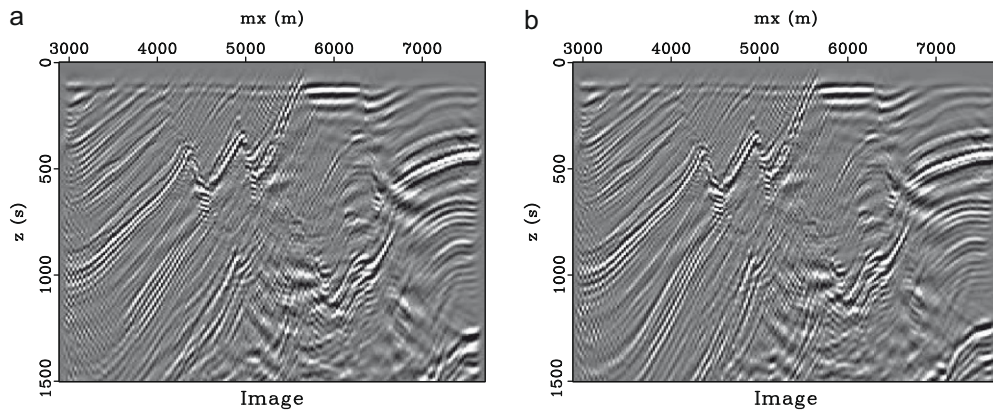**Fig. 11.** Dix velocity in depth (a) and estimated velocity (b).

Fig. 12. (a) Prestack depth migration using Dix velocity. (b) Prestack depth migration using estimated velocity.

7. PDE for Q in 3D

Similar to the two-dimensional case, we can derive a time domain PDE for $\mathbf{Q}$ in 3D. The evolution equations for $\mathbf{Q}$ and $\mathbf{P}$ are given by (see [18])

$$
\begin{aligned}
\mathbf{Q}_t &= v^2 \mathbf{P}, \\
\mathbf{P}_t &= -\frac{1}{v} \mathbf{V} \mathbf{Q},
\end{aligned}
\tag{61}
$$

where $\mathbf{V} = (v_{q_i q_j})_{i,j=1,2}$ is the matrix of the second derivatives of the velocity along the directions $\vec{e}_1$ and $\vec{e}_2$ which evolve along each image ray according to

$$
\frac{d\vec{e}_1}{dt} = v_{q_1}\vec{\tau}, \quad \frac{d\vec{e}_2}{dt} = v_{q_2}\vec{\tau}.
$$

Here $\vec{\tau}$ is a tangent vector to the image ray. By definition, the matrix $\mathbf{Q}$ is

$$
\mathbf{Q} \equiv \begin{pmatrix} \frac{\partial q_1}{\partial x_0} & \frac{\partial q_1}{\partial y_0} \\ \frac{\partial q_2}{\partial x_0} & \frac{\partial q_2}{\partial y_0} \end{pmatrix} \equiv \begin{pmatrix} R & S \\ T & U \end{pmatrix}.
\tag{62}
$$

We observe that

$$
\begin{pmatrix} \frac{\partial}{\partial x_0} \\ \frac{\partial}{\partial y_0} \end{pmatrix} = \mathbf{Q}^T \begin{pmatrix} \frac{\partial}{\partial q_1} \\ \frac{\partial}{\partial q_2} \end{pmatrix}, \quad \text{or more compactly,} \quad \nabla = \mathbf{Q}^T \nabla_{\mathbf{q}},
$$

where ∇ is the gradient w. r. t. (x_0, y_0), and $\nabla_{\mathbf{q}}$ is the gradient w. r. t. (q_1, q_2). Therefore,
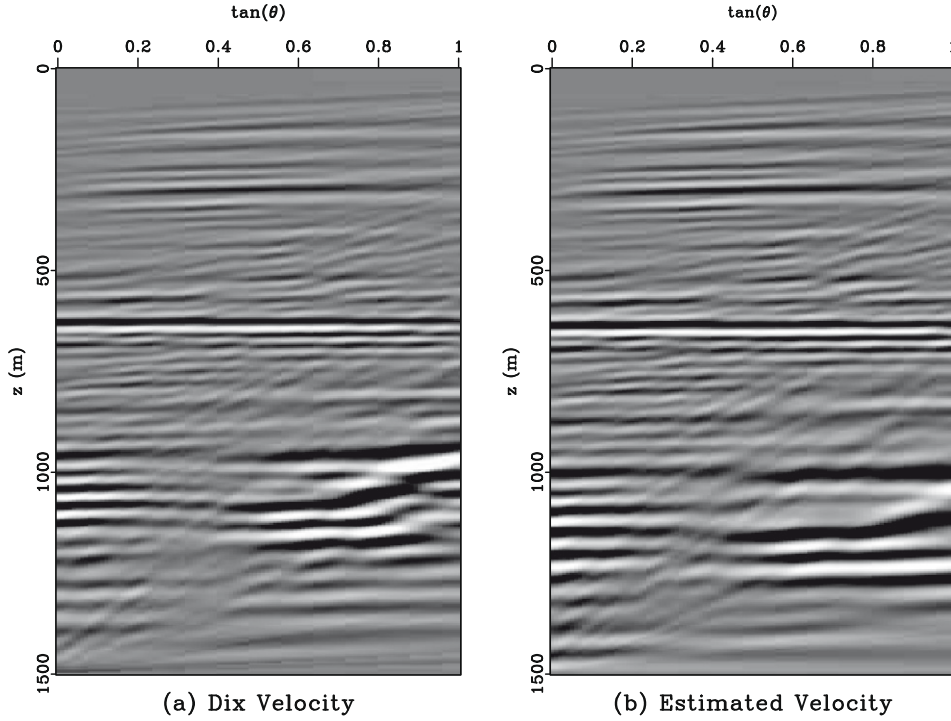
Fig. 13. Angle-domain common-image point gather at 4000 m using Dix velocity (a) and estimated velocity (b).

$$\nabla_{\mathbf{q}} = (\mathbf{Q}^T)^{-1}\nabla.$$

Hence

$$\mathbf{V} \equiv \begin{pmatrix} \frac{\partial^2 v}{\partial q_1^2} & \frac{\partial^2 v}{\partial q_1 \partial q_2} \\ \frac{\partial^2 v}{\partial q_2 \partial q_1} & \frac{\partial^2 v}{\partial q_2^2} \end{pmatrix} = \nabla_{\mathbf{q}}(\nabla_{\mathbf{q}} v)^T = (\mathbf{Q}^T)^{-1}\nabla((\nabla v)^T \mathbf{Q}^{-1}).$$

Thus, system (61) can be transformed into the following system of PDE's in the time coordinates:

$$\mathbf{Q}_t = v^2 \mathbf{P},$$ (63)

$$\mathbf{P}_t = -\frac{1}{v}(\mathbf{Q}^T)^{-1}\nabla[(\nabla v)^T \mathbf{Q}^{-1}]\mathbf{Q},$$ (64)

where the gradients are taken with respect to the coordinates x_0 and y_0.

According to the result proven in [3],

$$\mathbf{F} = v^2(\mathbf{Q}^T\mathbf{Q})^{-1},$$ (65)

where (see Eq. (7))

$$\mathbf{F} \equiv \frac{\partial}{\partial t_0}(t_0\mathbf{V}_m^2(\mathbf{x}_0, t_0))$$ (66)

is the matrix of the 3D analogues of the Dix velocities.

Therefore, $v^2 I_2 = \mathbf{F}\mathbf{Q}^T\mathbf{Q}$ and hence,

$$v = \sqrt[4]{\det \mathbf{F}(\det \mathbf{Q})^2}.$$ (67)

Looking at system (63) and (64) and at Eq. (67) we see that the matrices **F** are not required as input. Instead, their determinants are enough for restoration of the seismic velocity v. Rewriting system (63) and (64) as a single PDE we get:

$$\left(\frac{1}{v^2}\mathbf{Q}_t\right)_t = -\frac{1}{v}(\mathbf{Q}^T)^{-1}\nabla[(\nabla v)^T \mathbf{Q}^{-1}]\mathbf{Q},$$ (68)

where the velocity v is given by Eq. (67).

8. 3D numerics

We solve Eq. (68) numerically in a manner similar to the 2D case. We first update the matrix $\mathbf{P} = (\frac{1}{v^2}\mathbf{Q}_t)$. Then we update the matrix $\mathbf{Q}$ using the trapezoidal rule.

The input data $f(x, y, t)$ are the 3D analogue of the Dix velocity squared

$$f(x, y, t) \equiv \sqrt{\det \mathbf{F}} \equiv \frac{v^2}{\det \mathbf{Q}}. \tag{69}$$

The finite difference scheme uses a 9-point stencil (Fig. 14(a)) in space and the Lax–Friedrichs averaging given by

$$P_{ij}^{k+1} = \frac{P_{i-1j}^k + P_{i+1j}^k + P_{ij+1}^k + P_{ij-1}^k}{4} - \frac{1}{v_{ij}^k} (\mathbf{Q}^{-T})_{ij}^k \begin{pmatrix} (\alpha v_x)_x + (\beta v_y)_x & (\gamma v_x)_x + (\delta v_y)_x \\ (\alpha v_x)_y + (\beta v_y)_y & (\gamma v_x)_y + (\delta v_y)_y \end{pmatrix}_{ij}^k \mathbf{Q}, \tag{70}$$

where α, β, γ and δ are the elements of $\mathbf{Q}^{-T} \equiv (\mathbf{Q}^T)^{-1}$. The derivatives in Eq. (70) are evaluated as follows:

$$(\mu v_x)_x \approx ((v_{i+2j}^k - v_{ij}^k)\mu_{i+1j}^k - (v_{ij}^k - v_{i-2j}^k)\mu_{i-1j}^k) \frac{1}{4\Delta x^2}, \tag{71}$$

$$(\mu v_x)_y \approx ((v_{i+1j+1}^k - v_{i-1j+1}^k)\mu_{ij+1}^k - (v_{i+1j-1}^k - v_{i-1j-1}^k)\mu_{ij-1}^k) \frac{1}{4\Delta x \Delta y}, \tag{72}$$

$$(\mu v_y)_x \approx ((v_{i+1j+1}^k - v_{i+1j-1}^k)\mu_{i+1j}^k - (v_{i-1j+1}^k - v_{i-1j-1}^k)\mu_{i-1j}^k) \frac{1}{4\Delta x \Delta y}, \tag{73}$$

$$(\mu v_y)_y \approx ((v_{ij+2}^k - v_{ij}^k)\mu_{ij+1}^k - (v_{ij}^k - v_{ij-2}^k\mu_{ij-1}^k) \frac{1}{4\Delta y^2}. \tag{74}$$

Then we update the matrix $\mathbf{Q}$ according to the trapezoidal rule

$$\mathbf{Q}_{ij}^{k+1} = \mathbf{Q}_{ij}^k + \frac{\Delta t}{2}((v^2)_{ij}^k \mathbf{P}_{ij}^k + (v^2)_{ij}^{k+1} \mathbf{P}_{ij}^{k+1}). \tag{75}$$

Since

$$v^2 = \det \mathbf{Q} \sqrt{\det \mathbf{F}}, \tag{76}$$

we obtain the following equation for updating $\mathbf{Q}$

$$\mathbf{Q}_{ij}^{k+1} = \mathbf{Q}_{ij}^k + \frac{\Delta t}{2}(\mathbf{P}_{ij}^k(v^2)_{ij}^k + \mathbf{P}^{k+1}f_{ij}^k \det \mathbf{Q}_{ij}^k). \tag{77}$$

We observe that this is a system of the form

$$\begin{aligned} R &= a_R + b_R \det \mathbf{Q}, \\ S &= a_S + b_S \det \mathbf{Q}, \\ T &= a_T + b_T \det \mathbf{Q}, \\ U &= a_U + b_U \det \mathbf{Q}. \end{aligned} \tag{78}$$

To solve it, we subtract the product of the second and the third equations from the product of the first and the fourth equations in system (78) and obtain a quadratic equation w. r.t. the det $\mathbf{Q}$

$$(b_R b_U - b_S b_T)(\det \mathbf{Q})^2 + (-1 + a_R b_U + a_U b_R - a_S b_T - a_T b_S)\det \mathbf{Q} + (a_R a_U - a_S a_T) \equiv A(\det \mathbf{Q})^2 + B\det \mathbf{Q} + C = 0. \tag{79}$$
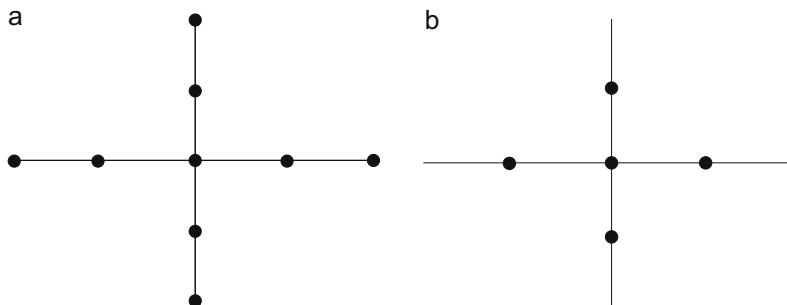

Fig. 14. Stencils used for the spatial discretization in 3D: (a) the 9-point stencil; and (b) the 5-point stencil.

We pick the root given by

$$\det \mathbf{Q} = \frac{2C}{-B + \sqrt{B^2 + 4AC}}, \tag{80}$$

which is consistent with the root 1 in the case where $\mathbf{Q} = 1, \mathbf{P} = 0$ and hence $A = 0, B = -1$ and $C = 1$. Then we can update the matrix $\mathbf{Q}$ substituting $\det \mathbf{Q}$ into Eq. (77).

8.1. Examples

The first 3D example is shown in Fig. 15. The exact velocity is

$$v(x, y, z) = 2 + 2e^{-0.15x^2 - 0.25y^2 - 0.15(z-2)^2}, \tag{81}$$

and the time domain is given by

$$-10 \leqslant x \leqslant 10, \quad -10 \leqslant y \leqslant 10, \ 0 \leqslant t \leqslant 1.5. \tag{82}$$

The seismic velocity distribution is shown on two vertical mutually orthogonal sections and a horizontal slice. The sections correspond to the planes $y = 0$ and $x = 0$. The depth of the horizontal plane is 2.55 km. The first column in Fig. 15 corresponds to the reconstructed velocity, the second – to the exact velocity, the third – the 3D analogue of the Dix velocity,
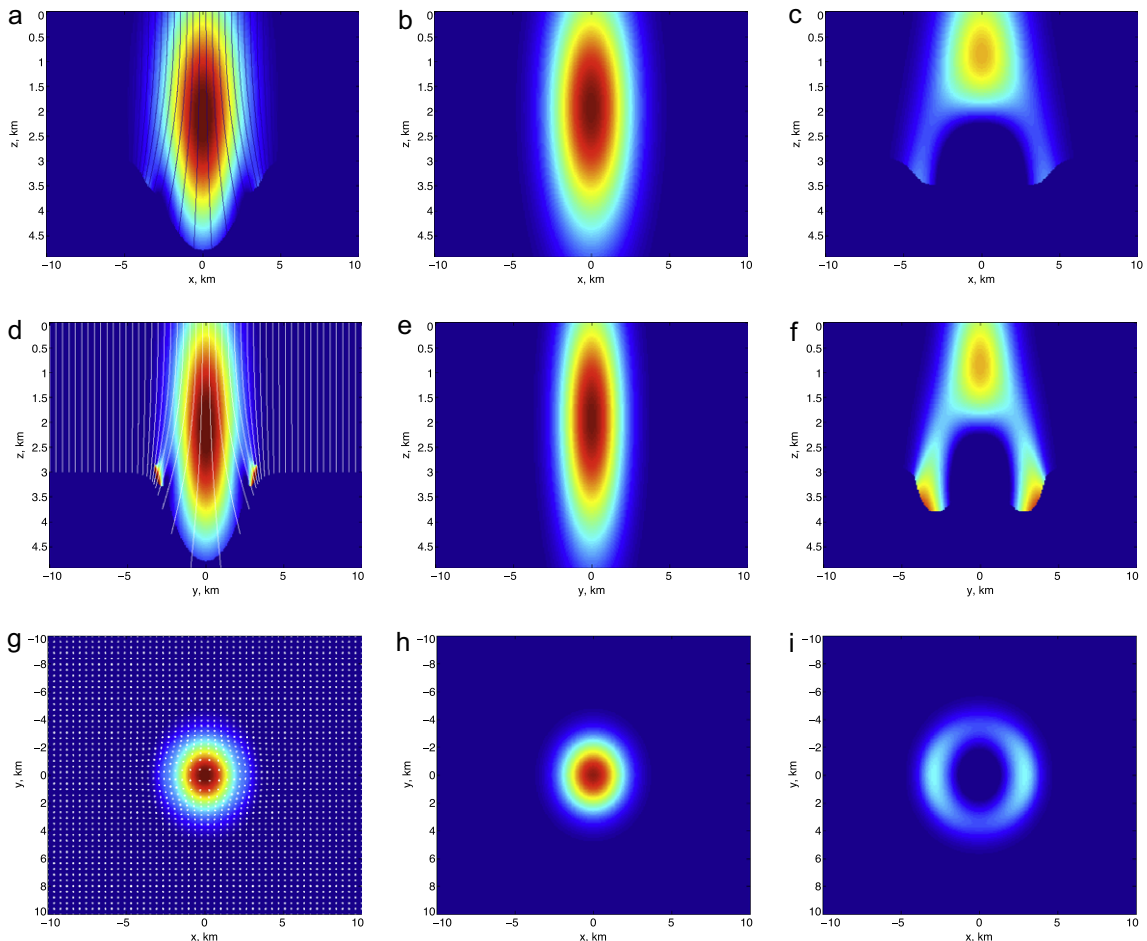

Fig. 15. 3D example 1. The first row: the velocity on the vertical plane $y = 0$. The second row: the velocity on the vertical plane $x = 0$. The third row: the velocity on the horizontal plane $z = 2.55$ km. The first column ((a), (d), and (g)): the reconstructed velocity and the image rays; the second column ((b), (e), and (h)): the exact velocity; the third column ((c), (f), and (i)): the velocity estimate analogous to Dix inversion, converted to depth. Dark blue (outer edges) and dark red (center) correspond to 2 km/s and 4 km/s, respectively. (For interpretation of the references to colour in this figure legend, the reader is referred to the web version of this article.)
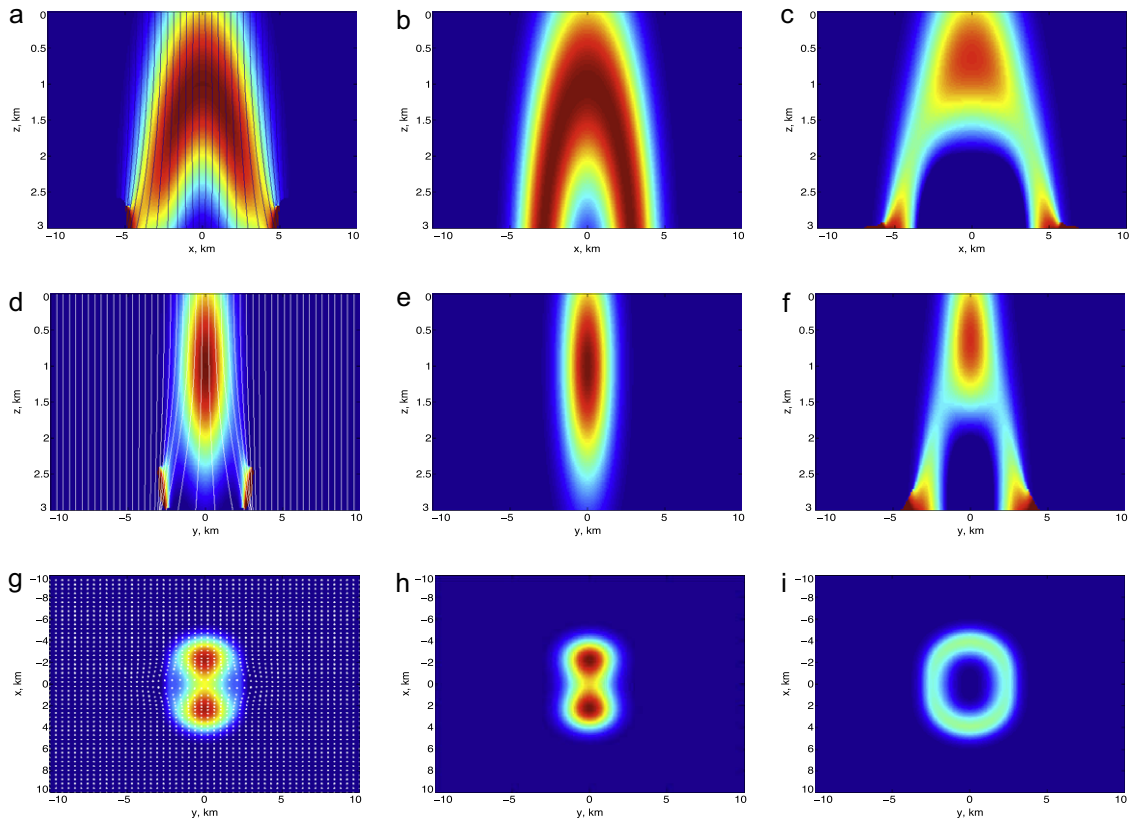
Fig. 16. 3D example 2. The first row: the velocity on the vertical plane $y = 0$. The second row: the velocity on the vertical plane $x = 0$. The third row: the velocity on the horizontal plane $z = 2.0$ km. The first column ((a), (d), and (g)): the reconstructed velocity and the image rays; the second column ((b), (e), and (h)): the exact velocity; the third column ((c), (f), and (i)): the velocity estimate analogous to Dix inversion, converted to depth. Dark blue (outer edges) and dark red (center) correspond to 2 km/s and 4 km/s, respectively. (For interpretation of the references to colour in this figure legend, the reader is referred to the web version of this article.)

converted to depth using our time-to-depth conversion algorithm. This example was computed on $500 \times 500 \times 500$ time-domain mesh. We see that our velocity correction by solving system (63) and (64) provides significant and qualitative improvement in comparison with the estimate similar to Dix inversion.[1]

The second 3D example is shown in Fig. 16. The exact velocity is

$$v(x, y, z) = 2 + 2e^{-0.4(d^2 + y^2)}, \tag{83}$$

where d is the distance from the upper semicircle given by

$$x^2 + (z - 4)^2 = 9, \quad z \leqslant 4, \; y = 0. \tag{84}$$

The time domain is given by

$$-10 \leqslant x \leqslant 10, \quad -10 \leqslant y \leqslant 10, \; 0 \leqslant t \leqslant 1.5. \tag{85}$$

The seismic velocity distribution is shown on two vertical mutually orthogonal sections and a horizontal slice. The sections correspond to the planes $y = 0$ and $x = 0$. The depth of the horizontal slice is 2.0 km. The first column in Fig. 16 corresponds to the reconstructed velocity, the second – to the exact velocity, the third – the 3D analogue of the Dix velocity, converted to depth using our time-to-depth conversion algorithm. This example was computed on 250×250 time-domain mesh. As in the previous example, our velocity correction by solving system (63) and (64) provides significant and qualitative improvement in comparison with the estimate similar to Dix inversion.

---

[1] The program used to compute the 3D examples in [3] overlooked the square root sign in the expression $v_{heur} = \frac{v}{\sqrt{\det \mathbf{Q}}}$ for the velocity estimate v_{heur} analogous to the Dix inversion. The text in [3] correctly states that $v_{heur} = \sqrt[4]{\det \mathbf{F}}$. This error did not affect our reconstruction but made the estimate v_{heur} which was only for reference appear worse than it should.

8.2. Error and perturbation analysis

As in the 2D case, we compare the following three schemes. The scheme with the 9-point stencil and the Lax–Friedrichs averaging, given by Eq. (70), a scheme with the same stencil but without the Lax–Friedrichs averaging, and a scheme with the 5-point stencil (Fig. 14(b)) and the Lax–Friedrichs averaging. These schemes are 3D analogues of the 2D schemes (23), (24), (55), (56), (58), and (59), respectively.

As in the 2D case, we derive the modified equations for the schemes. Then we perform the perturbation analysis for the original PDE for $\mathbf{Q}$ given by Eq. (68) and for the modified equations. For simplicity, let

$$\mathbf{F} = I_2 + \begin{pmatrix} \delta F_{11} & \delta F_{12} \\ \delta F_{21} & \delta F_{22} \end{pmatrix}. \tag{86}$$

Since the exact solution of Eq. (68) in the case $\mathbf{F} = I_2$ is the identity matrix $\mathbf{Q} = I_2$, the corresponding perturbed solution can be written in the form

$$\mathbf{Q} = I_2 + \begin{pmatrix} \delta R & \delta S \\ \delta T & \delta U \end{pmatrix}. \tag{87}$$

Then

$$v + \delta v = \sqrt[4]{\det \mathbf{F} (\det \mathbf{Q})^2} = 1 + \frac{1}{4}(\delta F_{11} + \delta F_{22}) + \frac{1}{2}(\delta R + \delta U). \tag{88}$$

After manipulations similar to those for 2D, we obtain the following equations for the perturbations of $\mathbf{Q}$:

$$\begin{aligned}
\delta R_{tt} + \frac{1}{2}(\delta R_{xx} + \delta U_{xx}) &= -\frac{1}{4}(\delta F_{11} + \delta F_{22})_{xx}, \\
\delta S_{tt} + \frac{1}{2}(\delta R_{xy} + \delta U_{xy}) &= -\frac{1}{4}(\delta F_{11} + \delta F_{22})_{xy}, \\
\delta T_{tt} + \frac{1}{2}(\delta R_{yx} + \delta U_{yx}) &= -\frac{1}{4}(\delta F_{11} + \delta F_{22})_{yx}, \\
\delta U_{tt} + \frac{1}{2}(\delta R_{yy} + \delta U_{yy}) &= -\frac{1}{4}(\delta F_{11} + \delta F_{22})_{yy},
\end{aligned} \tag{89}$$

Adding the first and the last equation and introducing a new variable $\xi \equiv \delta R + \delta U$ we come to the following equation for ξ.

$$\xi_{tt} + \frac{1}{2}\xi_{xx} + \frac{1}{2}\xi_{yy} = \mathcal{F}, \tag{90}$$

where

$$\mathcal{F} = -\frac{1}{4}(\delta F_{11} + \delta F_{22})_{xx} + \frac{1}{4}(\delta F_{11} + \delta F_{22})_{yy}. \tag{91}$$

Eq. (90) is a 3D Poisson equation and it has growing harmonics. Let $a(k, l, t)$ be the Fourier transform of $\xi(x, y, t)$ in x and y. Then the corresponding equation for a is

$$a_{tt} - \frac{1}{2}(k^2 + l^2)a = \widehat{\mathcal{F}}. \tag{92}$$

For the modified equation for the scheme with the 9-point stencil and the Lax–Friedrichs averaging we obtain the following equation for ξ:

$$\frac{\Delta t}{2}\xi_{ttt} + \xi_{tt} - \frac{\Delta x^2}{4\Delta t}\xi_{xxt} + \frac{\Delta y^2}{4\Delta t}\xi_{yyt} + \frac{1}{2}\xi_{xx} + \frac{1}{2}\xi_{yy} + \frac{1}{6}(\xi_{xxxx}\Delta x^2 + \xi_{yyyy}\Delta y^2) = \mathcal{F}. \tag{93}$$

The corresponding equation for the Fourier amplitudes is

$$\frac{\Delta t}{2}a_{ttt} + a_{tt} + \left(\frac{\Delta x^2}{4\Delta t}k^2 + \frac{\Delta y^2}{4\Delta t}l^2\right)a_t + \frac{1}{2}\left(\frac{k^4}{6} + \frac{l^4}{6} - k^2 - l^2\right)a = \widehat{\mathcal{F}}. \tag{94}$$

For the modified equation for the scheme with the 9-point stencil without the Lax–Friedrichs averaging we obtain the following equation for ξ:

$$\frac{\Delta t}{2}\xi_{ttt} + \xi_{tt} + \frac{1}{2}\xi_{xx} + \frac{1}{2}\xi_{yy} + \frac{1}{6}(\xi_{xxxx}\Delta x^2 + \xi_{yyyy}\Delta y^2) = \mathcal{F}. \tag{95}$$

The corresponding equation for the Fourier amplitudes is

$$\frac{\Delta t}{2}a_{ttt} + a_{tt} + + \frac{1}{2}\left(\frac{k^4}{6} + \frac{l^4}{6} - k^2 - l^2\right)a = \widehat{\mathcal{F}}. \tag{96}$$

For the modified equation for the scheme with the 5-point stencil and the Lax–Friedrichs averaging we obtain the following equation for ξ:

$$\frac{\Delta t}{2}\xi_{ttt} + \xi_{tt} - \frac{\Delta x^2}{4\Delta t}\xi_{xxt} + \frac{\Delta y^2}{4\Delta t}\xi_{yyt} + \frac{1}{2}\xi_{xx} + \frac{1}{2}\xi_{yy} + \frac{1}{24}(\xi_{xxxx}\Delta x^2 + \xi_{yyyy}\Delta y^2) = \mathcal{F}. \tag{97}$$

The corresponding equation for the Fourier amplitudes is

$$\frac{\Delta t}{2}a_{ttt} + a_{tt} + \left(\frac{\Delta x^2}{4\Delta t}k^2 + \frac{\Delta y^2}{4\Delta t}l^2\right)a_t + \frac{1}{2}\left(\frac{k^4}{24} + \frac{l^4}{24} - k^2 - l^2\right)a = \widehat{\mathcal{F}}. \tag{98}$$

Eqs. (94), (96), and (98) are analogous to Eqs. (52), (57), and (60), respectively. Hence the most stable scheme is Schemes (70) and (77). The other two schemes show less stability as it was in 2D.

9. Conclusions

In this work, we have established the mathematical properties of the problem of seismic velocity estimation from time migration, reduced it to a Cauchy problem for a partial differential equations in 2D and 3D. These PDEs bind the Dix velocity and the geometrical spreading of the image rays in 2D and 3D and allow us to reconstruct the seismic velocity from the input data (the Dix velocity). These PDEs are elliptic: they contain first and second derivatives of the Dix velocity as coefficients. The physical setting allows us to pose only a Cauchy problem for these PDE's, which is well-known to be ill-posed. Nevertheless, we have developed finite difference numerical schemes in 2D and 3D which contain an averaging loosely related to Lax–Friedrichs schemes. We have also adjusted a spectral Chebyshev method for the PDEs in 2D. With these, we have been able to estimate the seismic velocity in 2D and 3D quite accurately up to desired (shallow enough) depth.

We have applied an error and perturbation analysis to our finite difference schemes and showed that our averaging and the wide stencil in space lead to small error terms which suppressed the highest harmonics supported by the mesh for certain constant ratios of the grid step in space and in time. Our schemes do not suppress the lower harmonics, however, if the desired maximal time/depth is shallow enough (just a few kilometers), then lower harmonics do not grow significantly.

We have tested our results on a variety of two- and three-dimensional analytic examples and demonstrated dramatic improvement of the accuracy in comparison with the Dix inversion.

A test on the Marmousi synthetic dataset confirms the ability of our approach to improve the interval velocity estimates in comparison with the classic Dix inversion.

Acknowledgments

References

[1] J.P. Boyd, Chebyshev and Fourier Spectral Methods, second ed. (Revised), Dover Publications, INC, Mineola, New York, 2001.
[2] M.K. Cameron, S. Fomel, J.A. Sethian, Seismic velocity estimation and time-to-depth conversion of time-migrated images, SEG/New Orleans 2006 Technical Program Online (SVIP 1.7) <http://abstracts.seg.org/techprog.cfm?pMeetingID=3>.
[3] M.K. Cameron, S. Fomel, J.A. Sethian, Seismic velocity estimation from time migration, Inverse Problems 23 (2007) 1329–1369.
[4] M.K. Cameron, Seismic velocity estimation from time migration, Thesis, ProQuest, 2007.
[5] M.K. Cameron, S. Fomel, J.A. Sethian, Inverse problem in seismic imaging, PAMM 7 (1) (2007) 1024803–1024804.
[6] M.K. Cameron, S. Fomel, J.A. Sethian, Time-to-depth conversion and seismic velocity estimation using time-migration velocity, Geophysics 73 (2008) VE205.
[7] V. Červený, Seismic Ray Theory, Cambridge University Press, 2001.
[8] C.H. Dix, Seismic velocities from surface measurements, Geophysics 20 (1955) 68–86.
[9] S. Fomel, Time-migration velocity analysis by velocity continuation, Geophysics 68 (2003) 1662–1672.
[10] P. Hubral, Time migration – some ray theoretical aspects, Geophysical Prospecting 25 (1977) 738–745.
[11] P. Hubral, T. Krey, Interval Velocities from Seismic Reflection Time Measurements: SEG, 1980.
[12] E. Iversen, M. Tygel, Image-ray tracing for joint 3D seismic velocity estimation and time-to-depth conversion, Geophysics 73 (3) (2008) S99.
[13] M.V. Klibanov, F. Santosa, A computational quasi-reversibility method for Cauchy problems for Laplace's equation, SIAM Journal on Applied Mathematics 51 (1991) 1653–1675.
[14] G. Lambaré, Stereotomography, Geophysics 73 (2008) VE25.
[15] P.D. Lax, Weak solutions of hyperbolic equations and their numerical computation, Communication and Pure Applied Mathematics 7 (1954) 159–193.
[16] R.J. LeVeque, 1992. Numerical Methods for Conservation Laws, Basel, Boston, Berlin, Birkh auser, 1992.
[17] R.D. Richtmyer, K.W. Morton, Difference Methods for Initial-value Problems, Interscience Publishers, New York, 1967.
[18] M.M. Popov, Ray Theory and Gaussian Beam Method for Geophysicists, Salvador: EDUFBA, 2002.
[19] M.M. Popov, I. Pšenčík, Computation of ray amplitudes in inhomogeneous media with curved interfaces, Studia Geophysica et Geodaetica 22 (1978) 248–258.
[20] S.B. Fomel, P.C. Sava, Angle-domain common-image gathers by wavefield continuation methods, Geophysics 83 (3) (2003) 1065–1074.
[21] J.A. Sethian, A fast marching level set method for monotonically advancing fronts, Proceedings of the National Academy of Sciences 93 (1996) 4.
[22] J.A. Sethian, Fast marching methods, SIAM Review 41 (2) (1999) 199–235.
[23] J.A. Sethian, Level Set Methods and Fast Marching Methods, Cambridge University Press, 1999.

[24] J.A. Sethian, A. Vladimirsky, Ordered upwind methods for static Hamilton–Jacobi equations: theory and algorithms, SIAM Journal on Numerical Analysis 41 (1) (2003) 325–363.
[25] P. Shen, W.W. Symes, Automatic velocity analysis via shot profile migration, Geophysics 73 (2008) VE49.
[26] V.P. Singh, B. Duquet, M. Léger, M. Schoenauer, Automatic wave-equation migration velocity inversion using multiobjective evolutionary algorithms, Geophysics 73 (2008) VE61.
[27] W.W. Symes, Migration velocity analysis and waveform inversion, Geophysical Prospecting 56 (2008) 765–790.
[28] R. Versteeg, The Marmousi experience: velocity model determination on a synthetic complex data set, The Leading Edge 13 (1994) 927–936.
[29] M.J. Woodward, D. Nichols, O. Zdraveva, P. Whitfield, T. Johns, A decade of tomography, Geophysics 73 (2008) VE5.
[30] O. Yilmaz, Seismic Data Analysis: Soc. of Expl. Geophys., 2001.